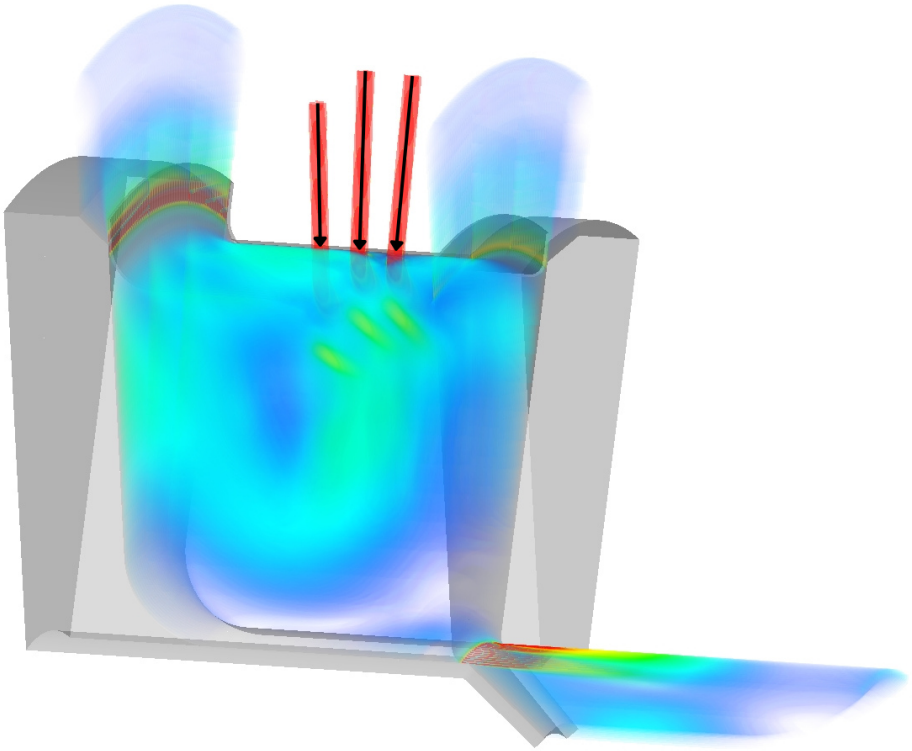

Heat Transfer in a Turbine Cavity

An Investigation into Correlation-Based Heat Transfer Compared to Computational Fluid Dynamics

Master's thesis in Mobility Engineering

ALRIK SJÖKVIST

DEPARTMENT OF MECHANICS AND MARITIME SCIENCES
CHALMERS UNIVERSITY OF TECHNOLOGY
Gothenburg, Sweden 2026
www.chalmers.se

Master's Thesis in Mobility Engineering

Heat Transfer in a Turbine Cavity

An Investigation into Correlation-Based Heat Transfer Compared to Computational Fluid Dynamics

ALRIK SJÖKVIST

CHALMERS
UNIVERSITY OF TECHNOLOGY

Department of Mechanics and Maritime Sciences
Division of Fluid Dynamics
Chalmers University of Technology
Gothenburg, Sweden 2026

Heat Transfer in a Turbine Cavity
An Investigation into Correlation-Based Heat Transfer Compared to Computational Fluid Dynamics
ALRIK SJÖKVIST

Supervisor: Jonas Sandblom, David Andersson & Alexander Rodin, GKN Aerospace
Examiner: Tomas Grönstedt, Mechanics and Maritime Sciences

Master's Thesis 2026
Department of Mechanics and Maritime Sciences
Chalmers University of Technology
SE-412 96 Gothenburg
Sweden
Telephone +46 31 772 1000

Cover: Meridional mass flow in three sectors with solid domains as shaded grey.

Typeset in LaTeX
Gothenburg, Sweden 2026

Heat Transfer in a Turbine Cavity
An Investigation into Correlation-Based Heat Transfer Compared to Computational Fluid Dynamics
ALRIK SJÖKVIST

Department of Mechanics and Maritime Sciences
Division of Fluid Dynamics
Chalmers University of Technology

Abstract

The Secondary Air System (SAS) is a vital component of modern gas turbine engines. As combustor outlet temperatures continue to increase, the cooling air supplied by the SAS is essential for maintaining component functionality throughout the flight envelope. Due to the critical role of cooling air, accurate thermal analysis of SAS components is required to assess component longevity. Although a validated Computational Fluid Dynamics (CFD) with conjugate heat transfer can model this problem with high accuracy, the computational cost makes such simulations impractical for full flight-cycle analyses. As an alternative, a thermal-only Finite Element Analysis (FEA) approach can be employed using estimated fluid flow behaviour. In this approach, convective heat transfer coefficients at fluid–solid interfaces are obtained using Nusselt number correlations. This work investigates the performance of different heat transfer correlations and evaluates their accuracy for an arbitrary turbine cavity. Overall, the correlations provided adequate temperature predictions for solid SAS components for a steady-state analysis. More specific correlations accounting for rotational effects yielded improved accuracy, in some cases predicting temperatures within a few degrees of those obtained from conjugate CFD simulations. To further improve accuracy, particularly within the fluid domain, the influence of the viscous sub-layer friction should be considered in the thermal model. In conclusion, this study demonstrates that, with careful selection of heat transfer correlations, good estimates of the SAS temperatures can be achieved using a thermal-only FEA approach. However, the accuracy of the method strongly depends on the quality of the underlying fluid flow estimations.

Keywords: Computational Fluid Dynamics (CFD), Finite Element Analysis (FEA), Conjugate Heat Transfer (CHT), secondary air systems, turbofan engines, heat transfer correlations, Nusselt number.

Preface

This report presents the outcome of my master's thesis project carried out at the Department of Mechanics and Maritime Sciences at Chalmers University of Technology during the spring of 2026. The thesis was completed in collaboration with GKN Aerospace in Trollhättan. It is the final work of my master's degree that has focused on the aerospace and fluid mechanics fields.

Acknowledgements

I would like to express my gratitude to my supervisors at GKN Aerospace Sweden, Jonas Sandblom, David Andersson, and Alexander Rodin, for their ongoing support and guidance throughout this master's thesis project. I also wish to thank GKN Aerospace for the opportunity to conduct my thesis here, especially the people at the Department of Aero–Thermal Analysis for making me feel welcome over the past few months. I am also grateful to Prof. Tomas Grönstedt for taking on the role of examiner for this thesis. Furthermore, I want to thank everyone at Chalmers University of Technology over the past years: the teachers for the knowledge they have imparted, and the students for making this an experience of a lifetime. Finally, none of this would have been possible without my family; thank you for your support and encouragement throughout my entire education.

Alrik Sjökvist, Gothenburg, June 2026

List of Acronyms

Below is the list of acronyms that have been used throughout this thesis, listed in alphabetical order:

BOI	Body of Influence
CDB	Coded Database (ANSYS APDL file)
CFD	Computational Fluid Dynamics
CHT	Conjugate Heat Transfer
FEA	Finite Element Analysis
FEM	Finite Element Method
FVM	Finite Volume Method
HPC	High-Pressure Compressor
HPT	High-Pressure Turbine
HTC	Heat Transfer Coefficient
LPT	Low-Pressure Turbine
RANS	Reynolds-Averaged Navier–Stokes
RDS	Rotating Disc System
RPM	Revolutions per Minute
SAS	Secondary Air System
SST	Shear Stress Transport

Nomenclature

Below is the nomenclature of indices, parameters, and variables that have been used throughout this thesis.

Indices

i, j	Cartesian coordinate indices ($i, j = 1, 2, 3$)
m	Meridional direction
r	Radial direction
s	Surface
x	Axial direction
θ	Tangential direction
∞	Free-stream / bulk value

Parameters

B	Empirical log-law constant [-]
c_p	Specific heat capacity [$\mathrm{J\,kg^{-1}\,K^{-1}}$]
h	Heat transfer coefficient [$\mathrm{W\,m^{-2}\,K^{-1}}$]
k	Thermal conductivity [$\mathrm{W\,m^{-1}\,K^{-1}}$]
κ	von Kármán constant [-]

Variables

Latin symbols

E	Total energy per unit mass [$\mathrm{J\,kg^{-1}}$]
f_i	Body force per unit mass [$\mathrm{m\,s^{-2}}$]
L	Characteristic length [m]

Nu	Nusselt number [-]
p	Pressure [Pa]
Pr	Prandtl number [-]
q	Heat flux [$\mathrm{W\,m^{-2}}$]
$\dot{q}$	Volumetric heat source [$\mathrm{W\,kg^{-1}}$]
$\dot{q}_l$	Heat input per unit length [$\mathrm{W\,m^{-1}}$]
Re	Reynolds number [-]
t	Time [s]
T	Temperature [K]
T^*	Dimensionless temperature [-]
U	Characteristic velocity [$\mathrm{m\,s^{-1}}$]
u	Velocity magnitude [$\mathrm{m\,s^{-1}}$]
u_i	Velocity component [$\mathrm{m\,s^{-1}}$]
u^+	Dimensionless velocity [-]
u_τ	Friction velocity [$\mathrm{m\,s^{-1}}$]
x	Spatial coordinate [m]
x_i	Cartesian coordinate component [m]
y	Wall-normal coordinate [m]
y^*	Dimensionless wall-normal coordinate [-]
y^+	Dimensionless wall distance [-]

Greek symbols

α	Thermal diffusivity [$\mathrm{m^2\,s^{-1}}$]
β	Swirl ratio [-]
μ	Dynamic viscosity [$\mathrm{Pa\,s}$]
ν	Kinematic viscosity [$\mathrm{m^2\,s^{-1}}$]
ρ	Density [$\mathrm{kg\,m^{-3}}$]
τ_{ij}	Viscous stress tensor component [Pa]
τ_w	Wall shear stress [Pa]
Φ	Viscous dissipation [$\mathrm{W\,m^{-3}}$]
ψ	Stream function [$\mathrm{m^2\,s^{-1}}$]
ε_{ij}	Levi–Civita tensor [-]
Ω	Angular velocity [$\mathrm{rad\,s^{-1}}$]

Vectors and matrices

$\mathbf{C}$	Thermal capacitance matrix [$\mathrm{J\,K^{-1}}$]
$\mathbf{K}$	Thermal conductance matrix [$\mathrm{W\,K^{-1}}$]
$\mathbf{Q}$	Nodal heat load vector [W]
$\mathbf{T}$	Nodal temperature vector [K]
$\dot{\mathbf{T}}$	Time derivative of nodal temperature [$\mathrm{K\,s^{-1}}$]

Contents

List of Figures

List of Tables

1

Introduction

This chapter introduces the basic jet engine principles and, more importantly, the Secondary Air System (SAS). It also introduces the purpose and goals of this thesis along with the demarcations that limit its scope.

1.1 Background

The principal jet engine was first introduced in the 1930s [1]. It consists of a fan, compressor, combustor, turbine, and nozzle, as seen from the RM12 engine in Fig. 1.1. Where the fan and compressor increase pressure and temperature, the combustor increases temperature further, and the turbine extracts work from the air before it is ejected through the nozzle. Fighter jet engines such as the RM12 also add an afterburner, which provides greatly increased thrust by burning significantly more fuel. The afterburner is seen as the second half of the RM12 engine. For more modern engines, the compressor and turbine have been divided into multiple spools that can rotate with different angular velocities [2]. Thus, the High-Pressure Turbine (HPT) drives the High-Pressure Compressor (HPC) at one RPM, and the Low-Pressure Turbine (LPT) drives the fan at another.

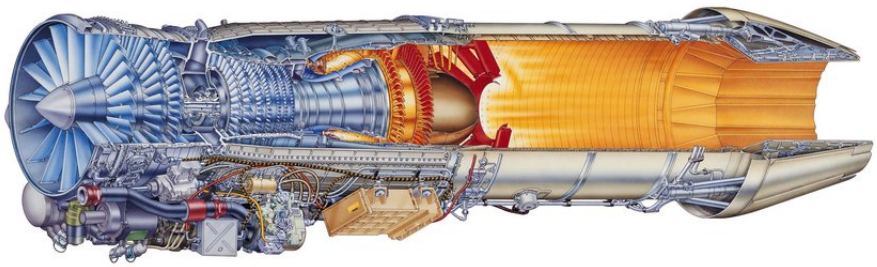

Figure 1.1: Illustration of the RM12 jet engine, courtesy of GKN Aerospace.

With the increasing performance of turbofan engines, an increase in the temperature out of the combustor follows. At take-off, the first turbine stage can experience temperatures of up to 2 000 K with hotspots a few 100 K above that [2]. To keep the engine parts, such as blades and guide vanes, from melting, cooling is introduced. Air is extracted from different stations in the fan and compressor, which is then used for the cooling of the turbine blades, pressurization of internal engine cavities,

and supplying pressurized air for a commercial airframe cabin.

This thesis will focus on these internal cavities that appear between different components, which play an important role in the longevity of the engine. However, it should be mentioned that the cavity in this thesis is fictional and has no actual connection to any specific SAS or jet engine in general. In its simplest form, these cavities can be expressed as a Rotating Disc System (RDS) [3], often with different rotational velocities from the aforementioned HPT and LPT. However, the flow inside these cavities can be complex, with multiple uncontrolled recirculation regions and significantly swirling flow. Swirl, in the context of an RDS, is the relation between the tangential velocity of a rotating disc and the fluid. Thus, to evaluate the longevity of the enclosing components, an accurate RDS model is necessary.

The lifespan of engine components relies on multiple factors, e.g. the stresses resulting from temperature gradients that occur within cavities. Thus, high resolution of the temperature field is desirable for accurate lifespan estimations. Using Computational Fluid Dynamics (CFD) to model the SAS and its cavities provides great accuracy when validated, but requires a large time investment. Consequently, simplified models are commonly used or developed to reduce the cost and time at the expense of accuracy in SAS analysis [4, 5, 6]. One method is to use correlations that evaluate the heat transfer between the complex air and solid parts of the cavity in a simplified manner.

In ANSYS Finite Element Analysis (FEA) software, the possibility exists to perform thermal analysis utilizing a simplified implementation of a fluid [7]. However, this implementation of a fluid excludes parts that are included in a CFD simulation. For example, the fluid internal friction, which is important for heat transfer, is not modelled by default in the FEA software. Instead, the option is available to specify internal sources of heat generation for the model.

1.2 Purpose

As stated in Sec. 1.1, the use and development of simplified models to evaluate the SAS is of great interest. With the high cost of CFD, especially time-wise, improving the accuracy of correlation-based models provides advantages in the development and evaluation of engines. Thus, the purpose of this thesis is to study a general RDS cavity to gain a greater understanding of the simplified model approach and how the fluid flow affects it. Here, the need to develop a way to implement the effects of internal friction in the fluid for the FEA is also necessary. Furthermore, the tangential velocity in the cavity and its effect on heat transfer is interesting to study; this is also known as swirl when it is related to the rotation of one of the discs. CFD simulations of the cavity will be performed and compared to correlation-based FEA to improve and evaluate its accuracy. Whilst the cavity in itself and its boundaries are fictional, the hope is to develop/improve an FEA model that applies to a range of different geometries. Ideally, such a model can then be used for with other boundary conditions without the need for CFD.

1.3 Goals

In regard to the stated purpose, the goal of this thesis is to answer the following questions:

- Do heat transfer correlations provide accurate results compared to CFD?
- How does swirl influence the heat transfer in the turbine cavity?
- How well does the implementation of fluid internal friction imitate the CFD?

1.4 Limitations

The scope of this thesis is limited to not creating any correlations, but rather only using correlations available from other researchers. Furthermore, no experimental validation of the CFD model will be made; hence, CFD will be considered the reference against which the FEA model is compared. The computational resources available are also limited; thus, there is a limit to how many or how long CFD simulations can be performed. Finally, the project is limited in licences available for commercial software, meaning there are potential constraints on what can be done during some steps of this thesis.

This means that the project will only utilize the ANSYS suite of products, such as ANSYS CFX for CFD and ANSYS Mechanical for meshing and thermal modelling. Open-source software such as Python is used for code development.

2

Theory

The following chapter will lay the theoretical foundation for the rest of the thesis. It introduces the fundamentals of heat transfer, some dimensionless parameters, rotating discs, and the chosen correlations, along with CFD and FEA.

2.1 Heat Transfer

Heat transfer between two bodies, either solid or fluid, occurs in three main forms. Those are conduction, convection, and radiation [8]. Their relevance depends on the specific problem in question, with conduction being most important in quiescent and slow moving flow, whilst convection becomes more important as the bulk fluid velocity increases. Radiation is heat transfer in the form of electromagnetic waves emitted from a solid or fluid. As a result, it works even without a transporting medium and is most prominent in a vacuum [8].

Conduction is the simplest form of heat transfer and occurs in bodies or between bodies in contact. It is the result of molecular vibration and collisions between them, transferring energy from more excited to less excited molecules. This is explained by Fourier's law:

$$q = -k\frac{\mathrm{d}T}{\mathrm{d}x} \tag{2.1}$$

where q is the heat flux, k is the thermal conductivity of the material and $\frac{dT}{dx}$ is the temperature gradient driving the heat transfer [8]. The negative sign is a result of the flux going from warmer to colder in accordance with the second law of thermodynamics.

The second mechanism for heat transfer is convection, and it is a result of fluid motion affecting the heat transfer as well as the individual motion of the molecules. The heat transfer resulting only from the bulk fluid motion is called advection, where convection is advection and conduction together [8]. The convection from a solid to a fluid, or vice versa, is explained by Newton's law of cooling:

$$q = h(T_s - T_\infty) \tag{2.2}$$

with h being a case-dependent Heat Transfer Coefficient (HTC) that is flow dependent and T_∞ being the bulk fluid temperature, i.e. the homogeneous temperature far from the wall [8]. Since convection includes both advection and conduction, it leads to higher heat transfer than conduction alone. Convection is further categorized into two types, natural and forced, where natural convection is buoyancy driven, and forced convection is a result of airflow from some external factor such as a fan or the wind [8].

If there is a difference between the wall temperature and the bulk fluid temperature, a thermal boundary layer will be present. This is a result of the fluid particles in contact with the wall being in thermal equilibrium with the wall, whilst the bulk fluid is either warmer or colder. Similarly to the kinematic boundary layer that is introduced later, there will be a temperature gradient away from the wall. By equating the conductive and convective wall heat-flux:

$$h = \frac{-k_f \, \partial T/\partial y|_{y=0}}{T_s - T_\infty} \tag{2.3}$$

it is seen that the HTC is directly related to this temperature gradient [8]. Where a thinner thermal boundary layer means a larger gradient and thus greater convective heat flux, and vice versa.

2.2 Dimensionless Parameters

Fluid flow is often categorized and evaluated using dimensionless numbers. It allows for very specific phenomena to be generalized and applied to other cases. The most common of these parameters is the Reynolds number (Re). It is defined as:

$$Re = \frac{\rho U L}{\mu} \tag{2.4}$$

with U and L being the characteristic velocity and length scales of the flow [9]. Re categorizes different flow regimes, with low Re indicating creeping flow, medium indicating laminar flow, and high Re indicating that the flow is turbulent. The exact ranges depend on the type of flow, e.g. cylinder flow or flow over a flat plate. In the case of solid rotation, such as for cylinders or discs, Re is often expressed as:

$$Re_\Omega = \frac{\rho \Omega r^2}{\mu} \tag{2.5}$$

this is known as the rotational Reynolds number Re_Ω, where Ω is the rotational velocity of the solid and r is the local radius. Thus, the radius is the characteristic length in this case, and the velocity is hidden in Ωr. What is special about Re_Ω is that it describes fluid flow from the solid motion, unlike the regular Re.

The second parameter is the Prandtl number (Pr). Unlike Re, Pr has no inherent scale in it. Rather, it is defined by the relation between the momentum diffusivity and the thermal diffusivity:

$$Pr = \frac{\nu}{\alpha} \tag{2.6}$$

where ν is the kinematic viscosity, or momentum diffusivity, and α is the thermal diffusivity [8]. Hence, Pr relates the kinematic and thermal boundary layers. For laminar boundary layers with little turbulent mixing, the Pr is related to the ratio of the kinematic boundary layer thickness to the thermal boundary layer thickness [8].

Lastly, the relation between the convective and conductive heat transfer, introduced in Sec. 2.1, can be explained by the Nusselt number [8], see Eq. (2.7). Where L is the characteristic length and k_f is the thermal conductivity of the fluid. This is an important dimensionless number which can be used to calculate the local value of h as a result of the normalized position, Re and Pr. There are many correlations that have been both mathematically and experimentally derived for the Nusselt number; see Sec. 2.4 for examples.

$$Nu \equiv \frac{hL}{k_f} = \left.\frac{\partial T^*}{\partial y^*}\right|_{y^*=0} \tag{2.7}$$

The Nusselt number is also equal to the dimensionless temperature gradient at the wall [8]. Thus, it is an important parameter in describing the thermal wall characteristics of the flow.

2.3 Rotating Flows

For a turbine cavity with multiple co-rotating parts of different rotational velocities, the flow will be influenced in different ways along different parts of the cavity. The physics relating to rotating flow as a result of rotating solids is presented in this section.

2.3.1 Rotating Discs

The simplest case for a rotating disc is that within a stationary fluid. As a result of the transfer of angular momentum from the disc to the fluid, the fluid will be pushed outwards in the radial direction, known as disc pumping. The radial outflow

of fluid induces an inflow in the axial direction [3]. The flow structure for the simple rotating disc in a stationary fluid is illustrated in Fig. 2.1.

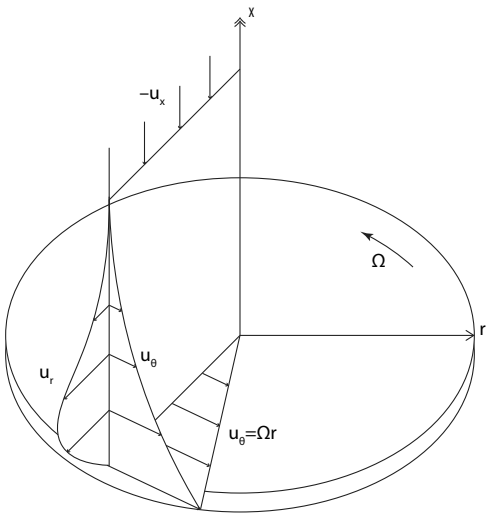

Figure 2.1: Flow over a rotating disc, adapted from [3].

The kinematic boundary layer that is created on this rotating disc may either be laminar or turbulent depending on multiple factors. Some investigations have indicated that the laminar boundary layer starts to break down when the local Re_Ω reaches 2×10^5 [3]. This is, of course, only an estimation, and the actual value depends on multiple conditions such as surface roughness and the specific flow field, but it gives an indication of the boundary layer turbulence. This also implies that the boundary layer will be turbulent further out and laminar towards the centre of the disc.

Another simple rotating disc case is that of a stationary disc and rotating fluid instead. It is the inverse of the earlier case, and the flow across it is as well. Rather than radial outflow, there will be inflow in the radial direction, resulting in axial outflow instead [3]. From the simple rotating disc cases, the jump to a more complex RDS can be made.

For flow between a rotor and an opposing stator, there are two different flow models. The first one was developed by Batchelor in 1951, and a competing one was developed by Stewartson in 1953. It has later been shown that Batchelor's is more applicable for an enclosed rotor-stator RDS, whilst Stewartson's better explains systems open to the atmosphere [3]. The Batchelor flow velocity profile from the rotor (R) to the opposing stator (S) is illustrated in Fig. 2.2.

The main thing proposed by Batchelor is the buildup of a boundary layer on the rotor and stator with a core of rotating fluid between the two discs. The lower velocity in the core compared to the rotor is explained by the swirl ratio, see Eq. (2.8) [3].

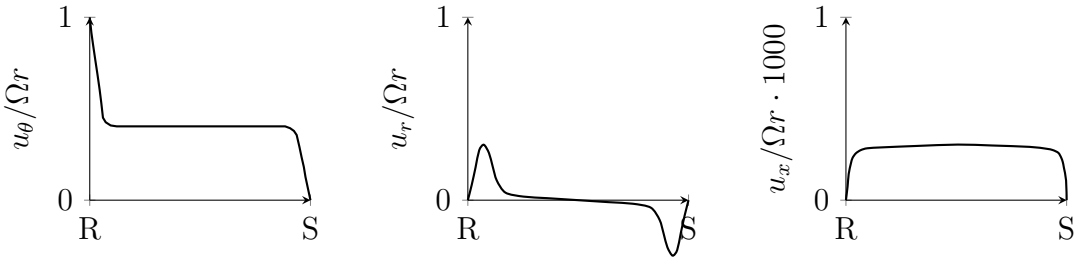

Figure 2.2: Batchelor flow velocity profiles for rotor-stator RDS, adapted from [3].

Where Ω_f is the rotational velocity of the fluid core, and Ω is the rotational velocity of the rotor. This ratio reduces as the distance between the two discs increases.

$$\beta = \frac{\Omega_f}{\Omega} \tag{2.8}$$

2.3.2 Rotating Cylinders

For a rotating cylinder in a quiescent fluid, a boundary layer will develop due to the velocity of the fluid gaining a velocity from the cylinder as a result of the no-slip condition. This boundary layer starts to observe instabilities for Re_Ω numbers as low as 40 to 60 in a quiescent fluid; a fully turbulent boundary layer appears later, and changes to the surrounding flow affect this limit as well [3]. When introducing a cross flow to the cylinder axis, the rotation reduces the velocity on one side and increases it on the other, curving the flow and causing lift; this is known as the Magnus–Robins force [9]. It is this that helps golf balls to fly further and has been used, and is used, to propel ships in place of a sail.

If there is flow inside a hollow cylinder with a smaller cylinder inside it, and they rotate at different rotational rates, a flow phenomenon called Couette flow occurs. Couette flow is the linear velocity profile created between a moving and fixed plate or rotating cylinders. The flow is dominated by viscous effects, and an analytical solution is possible [3]. The Couette flow solution is, however, only valid for incompressible flow and becomes unstable even at low cylinder rotational rates [9].

2.4 Nusselt Correlations

This section will introduce the correlations used in the thesis, how they were created and when they are valid. Due to the high Re_Ω of the cavity in this project, in the event that both are developed, the turbulent correlation will be presented.

2.4.1 Flat Plate

The simplest correlation is that for a flat plate; in this case, a correlation for turbulent flow over an isothermal plate is presented. Whilst the laminar correlation for parallel flow is analytically solvable, the turbulent case is not, since turbulent

flow is inherently chaotic. From experiments, the local friction coefficient has been approximated within 15% for Re numbers up to 10^8 [8]. The correlation is presented in Eq. (2.9), where Re_x is the local Re at location x along the plate. The correlation is valid for Pr between 0.6 and 60.

$$Nu = 0.0296 Re_x^{4/5} Pr^{1/3} \tag{2.9}$$

2.4.2 Rotating Disc

Whilst a flat plate is very general, a more specific correlation of a rotating disc might be applicable as well. For turbulent flow, it was first derived by Dorfman with a constant heat-flux boundary condition [10]. The correlation is for a free-rotating disc with convective flow over it and is shown in Eq. (2.10). It uses the local Re_Ω, evaluated at a radius r. How the correlation was derived by Dorfman is not found, but it is valid starting from a Re_Ω of 2.75×10^5 [10].

$$Nu = 0.0235 Re_\Omega^{0.8} Pr^{0.6} \tag{2.10}$$

2.4.3 Rotating Cylinder

There have been correlations made for rotating cylinders; however, most often using water as the convective medium. Therefore, the correlation is tested for Re_Ω numbers between 1×10^3 and 4.6×10^4, which is very low for a turbomachine. Similarly, Pr for this correlation is between 2.2 and 6.4, outside the typical range for air. The correlation is seen in Eq. (2.11) [11].

$$Nu = 0.11 Re_\Omega^{0.68} Pr^{0.4} \tag{2.11}$$

The experimental development of the correlation consists of a polished stainless steel tube submerged in water. It is heated via electrical resistance through the 300 mm long, 10.05 mm in outer diameter and 0.5 mm thick tube. The setup allows for approximately 3 000 Amperes, which is roughly 100 kW, to be supplied to the tube for heating [11]. The outside tube wall temperature, surface heat flux, water bulk temperature, and rotational speed of the tube are measured to obtain the dimensionless parameters. Whilst the experiment is carried out in water, it shows good correlation for air as well [11].

2.4.4 Turbine Disc

Some correlations are more specific to the problem at hand. One example is the correlation for a turbine disc presented in Eq. (2.12) [12]. It is developed for a Re_Ω between 2×10^5 and 1.2×10^6. Unlike the previous correlations, it relies only on Re and not Pr. Since it is experimentally derived, the effect of swirl is implicitly included in the correlation, and no consideration of it is made.

$$Nu = 0.0274 Re_{\Omega}^{0.8} \tag{2.12}$$

For this correlation development, the experiment consists of a rotating disc enclosed by two stationary casings, or stators, on either side. The two cavities are pressurized with air at a pressure of 620 kPa and a temperature of 21 °C to 25 °C. Air temperature is measured at the inlet and outlet of the cavity. The heat transfer surfaces of the disc consist of thin-walled copper rings along both sides. The rings are thermally isolated from each other to minimize conduction between them and have heaters on the backside, with the surface temperature measured at the fluid side of the rings. The disc surface temperature is kept at 55 °C throughout the experiment [12].

2.4.5 Rotor-Stator

Equation (2.13) is a correlation for a rotor-stator cavity [13]. As such, its derivation is for discs much closer together than other correlations. It is validated for Re_{Ω} numbers on the order of 10^5. The correlation should be valid in the outer half of an RDS cavity, but it depends on where the inlets and outlets are located.

$$Nu = 0.0195 Re_{\Omega}^{0.8} \tag{2.13}$$

By using the relative Re_{Ω} in the tangential direction, i.e. using the difference between the disc tangential velocity and fluid tangential velocity, swirl can be included [13]. In such cases, it acts as a damper on the regular Re_{Ω}, decreasing the HTC for this case; see Eq. (2.14). Since they are fitted to the same data, the two correlations show similar results.

$$Nu = 0.0074((1 - \beta) Re_{\Omega})^{0.89} \tag{2.14}$$

This setup consists of a stationary stator and rotating rotor discs close together, with vanes at the stator angling the airflow before it enters the cavity between them. The rotor is heated via a radiant heater on its backside with a capacity of 2 kW. The convective heat flux is measured on the rotor disc using a thermochromic liquid crystal coating and temperature measurements from probes embedded 7 mm from the surface. The air temperature is measured by small probes with a diameter of 0.2 mm [13].

2.5 Computational Fluid Dynamics

CFD is extensively used in engineering as a more in-depth analysis of complex fluid mechanics problems [14]. It utilizes the Finite Volume Method (FVM) compared to finite elements in FEA. This section will introduce the fundamental principles for how it works and the theory behind some choices made later.

2.5.1 Governing Equations

The base for all fluid dynamics, and what CFD solves, is the governing equations for fluid flow. They consist of the continuity, momentum, and energy equations seen in Eqs. (2.15a)–(2.15c) below [14]. The momentum equation is also known as the Navier–Stokes equation. They are derived for an infinitesimal, stationary control volume, but still large enough so that the fluid can be considered a continuum, and are thus presented in their conservative form. They are written in tensor form where E is the total energy and f_i is a body force; for all other parameters, see the Nomenclature section at the beginning. In steady-state simulations, the time-dependent terms are omitted from the equations.

$$\frac{\partial \rho}{\partial t} + \frac{\partial (\rho u_i)}{\partial x_i} = 0 \tag{2.15a}$$

$$\frac{\partial (\rho u_i)}{\partial t} + \frac{\partial (\rho u_i u_j)}{\partial x_j} = -\frac{\partial p}{\partial x_i} + \frac{\partial \tau_{ij}}{\partial x_j} + \rho f_i \tag{2.15b}$$

$$\frac{\partial (\rho E)}{\partial t} + \frac{\partial}{\partial x_j}\left(\rho E u_j + p u_j - u_i \tau_{ij} - \frac{\partial (kT)}{\partial x_j}\right) = \rho \dot{q} + \rho u_i f_i \tag{2.15c}$$

These equations are based on three fundamental physical principles [14]. The first one is that mass is conserved, meaning it can not be destroyed, only accumulated or redistributed. The second principle is Newton's second law [15], $F = ma$, which is the basis for the momentum equation. Lastly, there is the principle that total energy is conserved; it can not be destroyed, only change form; this is also known as the First Law of Thermodynamics [8].

For Conjugate Heat Transfer (CHT) simulations, heat transfer in solid regions must be computed instead of the three fluid governing equations. This is governed by Eq. (2.16) assuming no heat source inside the domain and is a version of Eq. (2.1) presented earlier [16].

$$\rho c_p \frac{\partial T}{\partial t} = \frac{\partial}{\partial x_i}\left(k \frac{\partial T}{\partial x_i}\right) \tag{2.16}$$

Viscous Dissipation

The viscous dissipation, see Eq. (2.17), appears in the energy equation, see Eq. (2.15c), and is an irreversible transformation of kinetic energy to thermal energy [17]. It is the result of viscous work, or friction, in the fluid from shear stresses. As a result, it is most prominent in high velocity gradient areas, such as near walls or recirculation regions.

$$\Phi = \tau_{ij}\frac{\partial u_i}{\partial x_j} = \mu\frac{\partial u_i}{\partial x_j}\frac{\partial u_i}{\partial x_j} \tag{2.17}$$

2.5.2 Fluid–Solid Interface

When performing CHT simulations, the interfaces between solid bodies and the fluid domain are important. The interfaces in themselves are treated as regular walls, but some specific conditions are applied relating to CHT. The temperature across the interface needs to be continuous, and the heat flux conserved [18]. Since the interfaces are walls, a no-slip condition also has to be applied, meaning the relative velocity between the wall and the fluid is zero [14]. For example, if the wall has a tangential velocity, so does the fluid in contact with it.

Boundary Layer Treatment

Due to the wall relative velocity of the fluid being zero at the wall and non-zero away from it, a velocity gradient in the fluid will be present. This is known as the kinetic boundary layer and, depending on the turbulence model, requires either to be resolved or modelled; see Sec. 2.5.3 for more information. Commonly, it is described by two dimensionless quantities, the first one:

$$u^+ = \frac{u(y)}{u_\tau} \tag{2.18}$$

where u_τ is the friction velocity and $u(y)$ is the velocity away from the wall assuming y is orthogonal to said wall [9, 14]. The second quantity is:

$$y^+ = \frac{u_\tau y}{\nu} \tag{2.19}$$

and is a dimensionless distance from the wall [9, 14]. Equations (2.18) and (2.19) describe the behaviour of the boundary layer. Furthermore, the friction velocity is defined according to:

$$u_\tau = \sqrt{\frac{\tau_w}{\rho}} \tag{2.20}$$

where τ_w is the wall shear stress. The boundary layer, and thus also the relation between u^+ and y^+, is divided into three main regions.

The first region is closest to the wall and is known as the viscous sub-layer; here, the value of $y^+ < 5$ and viscous forces dominate the flow. In this region u^+ and y^+ follow a linear relation according to Eq. (2.21) [9]. For y^+ values between 30 and 500, the relation between it and u^+ is logarithmic; hence, this is called the log-law

region, see Eq. (2.22). Where κ is Von Kármán's constant and B is an empirical constant, usually 0.41 and 5, respectively [9].

$$u^+ = y^+ \tag{2.21}$$

$$u^+ = \frac{1}{\kappa} ln(y^+) + B \tag{2.22}$$

The region between the viscous sub-layer and the log-law regions is called a transition or buffer region. Here, there is no equation to explain the velocity, and it is where it transitions from a linear relation to a logarithmic relation [9]. As a result, this region is hard to model, and it is recommended to keep y^+ outside this range. This is done by the first cell layer away from the wall either being small enough to resolve the inner boundary layer or large enough to accurately model it [14].

2.5.3 Turbulence Modelling

Whilst a lot of early fluid mechanics assumes laminar flow, this is rarely the case. Almost all actual flow is turbulent and thus requires either a very fine mesh to resolve it or models to estimate it. Resolving all turbulent scales is computationally expensive and outside the scope of this thesis. The need for modelling turbulence comes from the averaging of the governing equations. When performing Reynolds-Averaged Navier–Stokes (RANS) simulations, the act of averaging the equations in Sec. 2.5.1 introduces a stress tensor called the Reynolds stress tensor [17]. It is because of this that turbulence models are needed to close the governing equations.

As mentioned earlier, there are two types of turbulence models that handle the boundary layer differently. These are low-Reynolds approaches, which require resolving the boundary layer, and high-Reynolds approaches, which model the boundary layer [14, 17]. ANSYS CFX has multiple turbulence models available, with the three most common being the Shear Stress Transport (SST) model, the k-ε model and the k-ω model.

The k-ε model gets its name from using the turbulent kinetic energy (k) and the dissipation (ε) to close the governing equations. It is a high-Reynolds model, meaning it needs to model the wall behaviour, decreasing accuracy. It also has poor performance in flows with an adverse pressure gradient due to too low dissipation [17]. In comparison to this, the k-ω model is a low-Reynolds model, better handling wall behaviour compared to k-ε. It also does not have the same problems with adverse pressure gradients as a result of using the specific dissipation (ω), predicting lower shear stresses [17]. However, it is not as good with free-stream turbulence.

The SST model improves on this by using the k-ε model in the outer boundary layer and free stream, and the k-ω model in the inner boundary layer. This is done with the use of a blending function which smoothly switches between the two models as

the distance from the wall increases [17]. This also means it is a low-Reynolds model, meaning the resolution of the mesh at the wall is important, and its y^+ value should be around or below one. All the models mentioned here are isotropic, meaning they assume uniform properties in all directions.

2.5.4 Mass Flow Distribution

Since the continuity and momentum equations are coupled, they need to be solved simultaneously. This can be addressed by introducing the stream function. It satisfies continuity and allows for solving the momentum equation directly [9]. However, it requires a few simplifications to reduce the continuity equation from Eq. (2.15a) down to two terms. These are that it has to be steady-state, incompressible, and two-dimensional flow. From that, the stream function can be written as [9]:

$$u_i = \varepsilon_{ij} \frac{\partial \psi}{\partial x_j} \tag{2.23}$$

on tensor form in two dimensions where ψ is the stream function and ε_{ij} is the Levi–Civita tensor. The stream function is also useful in evaluating the flow. Streamlines are the lines along which the stream function is constant and are a common post-processing step used in CFD to visualize the flow structure. Furthermore, the change in the stream function across an element is equal to the volume flow through said element. Thus, the difference in the stream function between two streamlines is the volume flow between them [9].

The stream function is a great tool to visualize the flow distribution for a two-dimensional, incompressible and steady flow. Problems arise with more complex three-dimensional compressible simulations. Since ANSYS CFX does not provide a stream function for these more complex simulations and has no easy way to integrate within its post-processing environment, a simplified version has to be created to try to achieve the same result. Equation (2.24) shows this simplified version.

$$\psi_{3D} = \rho u_m \tag{2.24}$$

It is built similarly to the regular stream function utilizing the meridional velocity (u_m). However, unlike the stream function, the absolute values here are irrelevant, and it is the relation between them that is important.

2.6 Finite Element Analysis

Whilst CFD solves the equations using the FVM, FEA takes another approach, utilizing the Finite Element Method (FEM). One difference between FVM and FEM is that FVM integrates the governing equations over a control volume, whilst FEM uses a weak formulation of the heat transfer equation [16].

2.6.1 Finite Element Formulation

The governing equation for heat transfer in FEA is the same as in CHT simulations, see Eq. 2.16, repeated here:

$$\rho c_p \frac{\partial T}{\partial t} = \frac{\partial}{\partial x_i}\left(k \frac{\partial T}{\partial x_i}\right) \tag{2.25}$$

in the case of some internal heat generation, a source term matching this generation can be added, and for steady-state, the time-dependent term is excluded [16]. This governing equation is of a second order and, as in CFD, is not analytically solvable. This, along with boundary conditions, is also known as the strong form of the equation.

The solution to this in FEM is often multiplying the strong form equation by a test function and then integrating it over the domain. This results in the solvable weak form equation and is known as the Galerkin method. In FEM, the solution field is approximated using trial functions; what Galerkin suggests is to set the test functions equal to the trial functions [16]. This results in one equation per degree of freedom; in the case of temperature, one equation per node. The system of algebraic equations can then be written as:

$$\mathbf{KT} = \mathbf{Q} \tag{2.26}$$

on matrix form where $\mathbf{K}$ is the conductance matrix, $\mathbf{T}$ is the solution vector and $\mathbf{Q}$ is a load vector [16]. The solution vector can then be solved using regular matrix operations.

Fluid Elements

ANSYS provides the option to simulate simplified heat transfer in pipes, utilizing the fluid elements, to set the bulk fluid temperature needed in Eq. (2.2). The transport of thermal energy inside the one-dimensional pipes is written [8, 19]:

$$\rho c_p A \frac{\partial T}{\partial t} + \dot{m} c_p \frac{\mathrm{d}T}{\mathrm{d}x} = \dot{q}_l \tag{2.27}$$

where the first term is transient and excluded in steady-state simulations. The second term is the convective transport of the temperature along the pipe length as a result of the mass flow. For implementation, this is integrated over the pipe length and written in matrix form as [19]:

$$\mathbf{C}\dot{\mathbf{T}} + \mathbf{KT} = \mathbf{Q} \tag{2.28}$$

where **Q** is internal heat generation. It is here that, for example, the heat from internal fluid friction is added, and where the effects of convection between the fluid and solids take place. The temperature is solved at the nodes of the fluid pipe element used in the convective boundary condition for the solid elements.

2.6.2 Boundary Conditions

As in CFD, boundary conditions are required to obtain a unique solution to the partial differential equation. For the FEM, the different boundary conditions are often classified into different types.

Dirichlet Boundary

For Dirichlet boundary conditions, the temperature is specified at the boundary. This means the solution to the system of equations is constrained at these nodes. However, the temperature itself can vary along the boundary [16].

Neumann Boundary

On a Neumann boundary, the gradient of, in this case, temperature, over the boundary is specified. For example, a known heat-flux condition applied on a boundary falls under this definition. Just like the temperature, this can vary spatially along the boundary [16].

Robin Boundary

The last type of boundary condition is the Robin boundary, also called mixed. It is a combination of both Dirichlet and Neumann boundary conditions. The convective heat-flux boundary falls under this category since the conductive flux at the wall has to be equal to the convective flux [16]. This Robin boundary condition is thus included directly in the weak form equation.

In ANSYS, a convective boundary utilizes a surface element which integrates with the weak form equation [7]. This element can then connect with the fluid element to use information from it for the bulk fluid temperature in the convection equation, Eq. (2.2).

3

Methods

This chapter describes the methodology of the project, motivating the reason behind some choices made. It consists of CFD, implementing correlations in FEA and then comparing the results from both FEA and CFD.

3.1 Computational Fluid Dynamics

CFD simulations require multiple steps that will be introduced in this chapter. It is important to accurately set up the domain and physics to capture the desired phenomenon well. This is later evaluated to ensure physically correct results. The CFD simulations are performed using the ANSYS suite of products with CFX as the solver.

3.1.1 Setup

The setup of CFD is a balancing act between accuracy and computational cost. For instance, a finer mesh improves accuracy, but increased resolution may not be necessary across the entire domain. Similarly, there are simplifications which can be made to the physics and scope of the simulation to reduce cost without a significant decrease in accuracy. How everything was set up, along with some of these considerations, is presented in this section.

Geometry Preparations

The geometry is seen, with the rotating axis not to scale, in Fig. 3.1. Solids are represented by hatched areas, and different types of hatching indicate different mesh types. The provided geometry includes only the solid parts: the left solid being the HPT rotor, the right being the LPT rotor, and the top thin solid being a stator with a circular inlet at the centre. The fluid was created from this to fill the cavity created by the three solids. Between the solid parts are small seal clearances ranging from 0.18–0.6 mm in size; this is seen in detail X in the figure. The overall size of the cavity is approximately 10 cm across, with the inlet (A) being 6 mm in diameter.

The inlets and outlets (B–D) are elongated to ensure no effect on the relevant domain, and the outlets are converged to mitigate the risk of backflow through them.

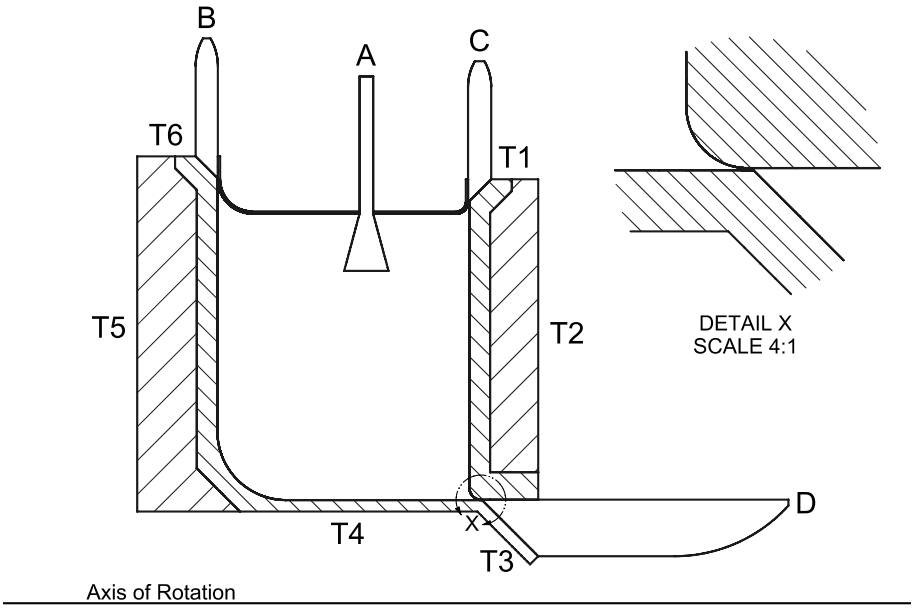

Figure 3.1: Domain for CFD, solids are shown as hatched areas.

The cone shape in the middle is a Body of Influence (BOI) used to locally refine the mesh around the inlet hole. Similar BOIs are created at the three seal clearances to ensure adequate cell count across them. Lastly, the HPT and LPT rotors are each divided into two bodies to allow for different mesh types for different regions.

Since the geometry is revolved around a central axis, running from left to right, it allows for simulating only a smaller section of it. In this case, a section with only one inlet is chosen. With a total of 30 inlets all along the circumference of the domain, each sector is 12°. This allows for greatly reduced computational resources required for the simulation.

Mesh

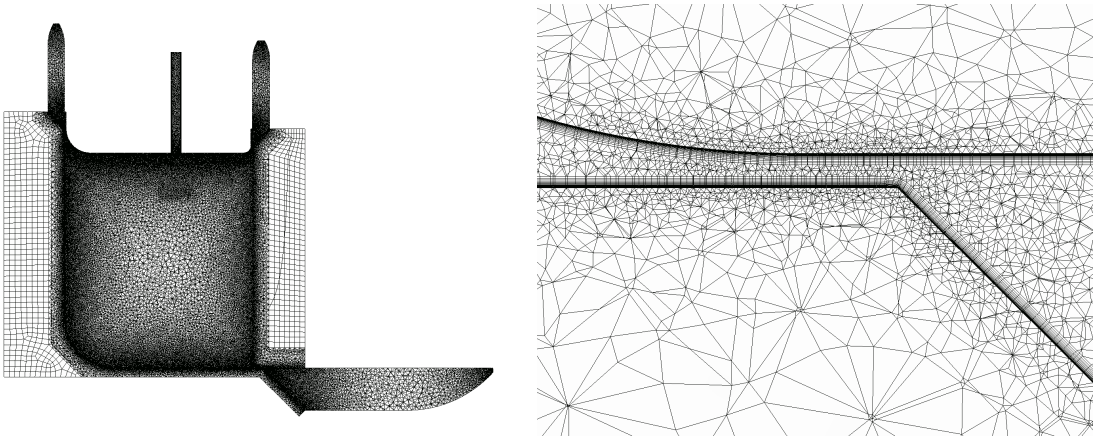

Figure 3.2: Mesh used in CFD, entire domain (left), close-up on clearance D (right).

The mesh is divided into two different cell types and is shown in Fig. 3.2. Tetrahedral cells are used for the fluid and parts of the solid in contact with it, and hexahedral cells for the outer part of the HPT and LPT rotors; this division can be seen in the figure. Ideally, the entire mesh should consist of hexahedral cells, but due to limitations in software and licences, it is not possible. A conformal mesh is used so that the nodes connect between the different mesh regions. The final mesh has a base size of 3 mm, with the seal clearance refinement zones setting a target size of five cells across the clearance gap. The inlet is refined to have six cells across it. The overall growth rate in the fluid is 1.25, and in the solids it is 1.4. For the general sizing of the mesh, see Table 3.1.

Table 3.1: General settings used for the final mesh.

Region	Size [mm]	Growth Rate
Fluid	3	1.25
Solid	3	1.4
Inlet	1	1.25
Clearance B	0.04	1.1
Clearance C	0.12	1.05
Clearance D	0.036	1.05

Capturing the boundary layer is done with the use of inflation layers. They are placed on the interfaces between the fluid and the solids. The mesh is also refined on the interfaces to ensure a smooth transition between the structured inflation layers and the regular mesh. The final mesh used between 18 and 25 layers, with a total thickness for the seal clearances of one third of the gap and a growth rate of 1.2. The total thickness for the main parts of the solids is based on the wall normal gradient of the tangential velocity and is thus an iterative process. The final settings used for the inflation layers are presented in Table 3.2.

Table 3.2: Inflation layer settings used for the final mesh.

Interface	Total Thickness [mm]	Number of Layers
HPT	0.5	25
LPT	0.4	18
Stator	0.4	20

Boundary Conditions

The provided boundary conditions for inlets, outlets and outer walls are presented in Table 3.3; the wall temperature locations (T1–T6) can be seen in Fig. 3.1. The temperature range over a single boundary indicates a linear relation. The inlet and outlet mass flows are scaled for the entire model, not just the single sector, i.e. the value provided needs to be divided by however many rotational sectors the entire model consists of. The interfaces between the fluid and solid domains employ a conservative heat flux over them to capture the flux across the wall between the fluid and solid. The HPT interface has a rotational velocity of 15 000 RPM, and the

LPT interface has a rotational velocity of 5 000 RPM, both in the negative direction given the axial direction from HPT to LPT.

Table 3.3: Initial mass flows, pressures and static temperatures at the boundaries; positive flow indicates inflow, negative flow indicates outflow.

Location	Mass Flow [g/s]	Pressure [kPa]	Temperature [K]
A	+410	950	650
B	–130	670	
C	–165	650	
D	–115	320	
T1			800
T2			550–800
T3			500
T4			500–650
T5			650–900
T6			900

Since the inlets and outlets are over-constrained and the values are not from experiments or requirements, the mass flow is used for mass flow boundaries and the pressure is used for pressure boundaries. To get a first solution, the inlet is set as a pressure inlet with the outlets at specified mass flows to ensure flow out of all of them. After a solution has propagated the entire domain, it is reversed with the specified mass flow at the inlet and the specified pressure at the outlets. The outlet pressures are modified during the run to achieve the desired mass flow at outlet C and so that the upstream seal clearance for outlet D is just about choked. Figure 3.3 shows the corrected values used in the simulations.

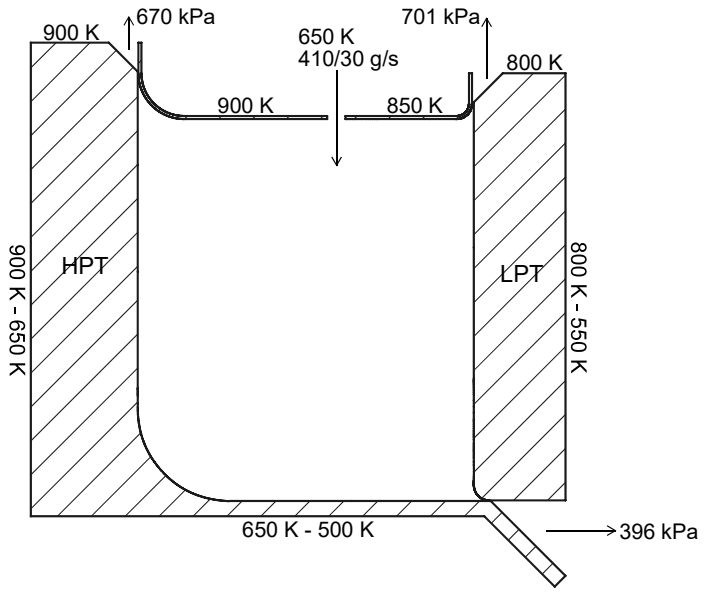

Figure 3.3: Corrected mass flows, pressures and temperatures at boundaries.

Physics Settings

The physics used in the CFD simulations is three-dimensional, steady-state, compressible, CHT, RANS, using ideal gas air for the fluid and Inconel 718 for the solids. Both materials are slightly modified, mainly regarding variability in thermal properties with temperature. The final physics settings used to achieve the results are presented in Table 3.4.

Table 3.4: Final physics settings used for CFD simulations.

Category	Setting Used
Space	Three-dimensional
Analysis Type	Steady-state
Fluid Model	Ideal Gas
Heat Transfer (Fluid)	Total Energy (with Viscous Work)
Heat Transfer (Solid)	Thermal Energy
Turbulence Model	SST
Numerical Schemes	High-resolution

Additional Cases

The effect of friction on the solution is investigated using a simplified model. The solids are removed, and only the fluid, with adiabatic walls, is simulated. The two cases compared are then with viscous work enabled and with it disabled in the turbulence model. The total temperature is studied for the two cases. This total temperature difference will be used to set an estimate for the required frictional heating to be implemented in the FEA model.

3.1.2 Model Validation

The validity of the model is evaluated by trying different cases with alternate temperatures on the wall. Since, according to Eq. 2.2, the flux is proportional to the temperature difference, the HTC should remain constant even if the temperature boundaries are changed. Two cases are tested and compared to the original one. For one case, the temperatures at the solid outer boundaries (T1–T6) are increased by 25 K and for the other, it is decreased by 25 K. See Sec. 4.1.2 for the results of this.

Mesh Sensitivity Study

To ensure that the CHT simulation provides accurate fluxes over the interfaces, an investigation into the inflation layers, and thus y^+, is made. The area-averaged heat flux is extracted from the stations outlined in Sec. 3.1.3. From this, the average value of h is calculated using Eq. (2.2) with the bulk fluid temperature set to the mean fluid in the middle of the cavity. The different peak y^+ values evaluated are 10, 3, 1, and 0.5. The total thickness needed for the inflation layers is investigated by the use of contour plots of the wall tangential velocity gradient in the normal

direction. The resolution of the boundary layer is evaluated from the wall tangential velocity in the normal direction, with the nodes displayed.

3.1.3 Fluid Post-processing

Initially, the interior cavity walls are divided into twelve different thermal zones over which the average HTC is calculated, as described earlier. The zones are defined to avoid significant fluctuations or changes in direction in wall heat flux across them. The numbering of the zones is illustrated for each solid individually in Fig. 3.4. These zones are used both for model validation and, more importantly, as division of the convective boundary for the FEA model.

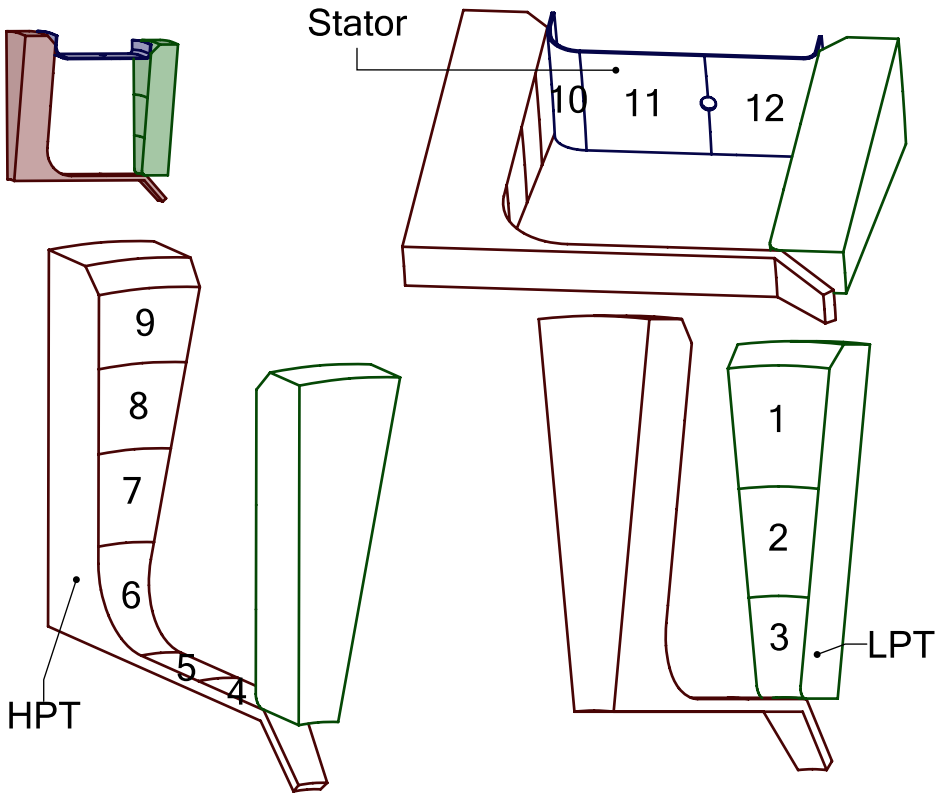

Figure 3.4: Numbering of the thermal zones on the HPT (left), LPT (right) and stator (top).

The other important result from the CFD is the distribution of mass flow in the fluid domain. It utilizes Eq. (2.24) to get quasi-streamline flow representation in 2D. This is used both to visualize the flow and as an aid when creating the fluid network for the FEA model. Perpendicular surfaces are created along the walls to evaluate the mass flow over the previously shown thermal zones, see Sec. 4.1. They are created using the distribution of mass flow as a guide.

Contours of other interesting parameters, such as temperature and velocity, are also used to evaluate the flow. Swirl is investigated by calculating the local swirl ratio along horizontal lines from the HPT to the LPT, separated by a quarter of the

domain height; their location is illustrated as horizontal lines in Fig. 3.5. Lastly, the temperature is probed at certain locations matching the FEA model for comparison, see Fig. 3.9 in Sec. 3.2.2.

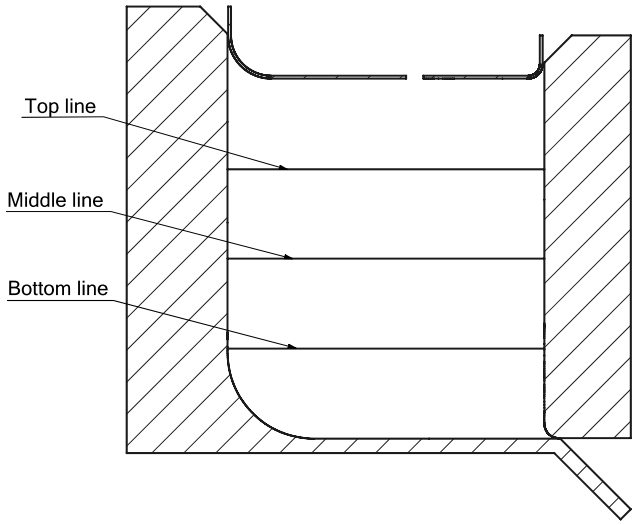

Figure 3.5: Location of the evaluation lines for swirl.

3.2 Finite Element Analysis

The FEA model is similar to the CFD model, albeit with a simplified fluid network to represent the fluid. The FEA analysis is performed using the ANSYS suite of products with ANSYS Workbench for the model creation and APDL as the solver. The correlation implementation is written in Python.

3.2.1 Setup

The setup of the FEA model includes multiple steps. The three main ones are the creation of the fluid network with the help of the CFD flow structure and mass flows, implementing the correlations for the convective boundary conditions, and the implementation of the frictional heating of the fluid.

Creation of Fluid Network

From the mass flow distribution of the CFD simulation, see Sec. 4.1, a fluid network is created consisting of ANSYS FLUID116 elements, see Fig. 3.6. This replaces the fluid from the CFD simulation, and it is used to set the temperature for the convective boundary condition in the FEA using SURF152 surface elements in ANSYS; the arrows indicate flow direction. Figure 3.6 also shows the general domain used for FEA. It is the same as in CFD, except there is no fluid body and the solids are not split into different mesh types.

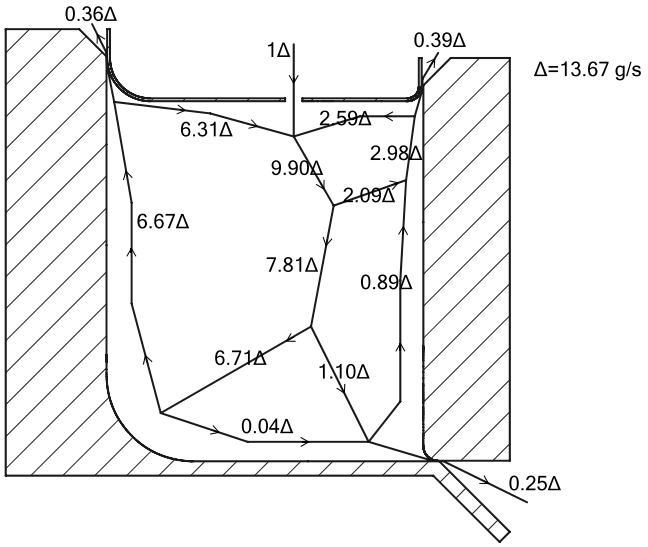

Figure 3.6: Fluid network for the FEA model.

Each fluid element in the FEA model is assigned a mass flow extracted from the CFD simulation, see Sec. 4.1. The mass flow for fluid elements in the middle of the cavity is calculated assuming mass balance. Each element mass flow is then presented as a factor of the inlet mass flow, allowing easy rescaling for different operating conditions.

Mesh

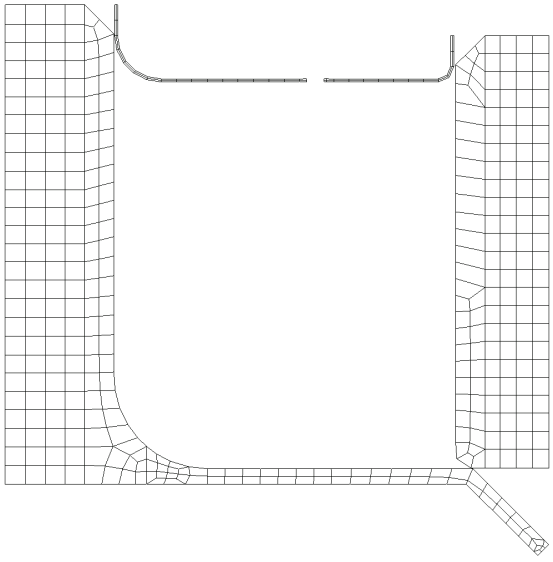

Figure 3.7: Mesh used for the FEA simulations.

The mesh used in the FEA model is coarser compared to the CFD model. It consists completely of hexahedral cells with no centre nodes. The fluid elements are meshed

with one cell per element. The mesh is made with the goal of having two cells across the stator, at least five cells across the rotors, with the smaller, bottom of the HPT rotor, having two cells across it as well. This is achieved utilizing edge sizing with the desired number of cells across the different edges of the solids and fluid elements. The growth rate is left at the default 1.85. The mesh is seen in Fig. 3.7.

Correlation Implementation

To apply the correlations, a script is written in Python which applies a correlation for each zone presented in Fig. 3.4 earlier. The script uses geometrical information from an ANSYS Mechanical CDB (Coded Database) file and fluid information from the CFD simulation. The script is divided into two main parts: the extraction of geometry and the implementation of correlations.

For each zone, the relevant geometrical data are extracted to get zone information for characteristic length, fluid node position, and more, after which a correlation is implemented for the zone from a selection of predetermined valid correlations; see Table 3.5. The correlation returns the Nusselt number, which is then used to get the HTC via Eq. (2.7). For the flat plate correlation, the HTC is calculated in every direction and then summed using the root-sum-squared method. For example, a zone along the LPT will have both a tangential and radial HTC component from the flat plate correlation. Meanwhile, for curved zones, e.g. zone 6, a radial and axial correlation is calculated and the mean of them is used in the FEA model. Example code is available in App. A.

Table 3.5: Mapping for what correlation is valid in which zone.

	Zone 1	**Zone 2**	**Zone 3**	**Zone 4**	**Zone 5**	**Zone 6**	**Zone 7**	**Zone 8**	**Zone 9**	**Zone 10**	**Zone 11**	**Zone 12**
Flat Plate Eq. (2.9)	✓	✓	✓	✓	✓	✓	✓	✓	✓	✓	✓	✓
Rotating Disc Eq. (2.10)	✓	✓	✓			✓	✓	✓	✓			
Rotating Cylinder Eq. (2.11)				✓	✓	✓						
Turbine Disc Eq. (2.12)	✓	✓	✓			✓	✓	✓	✓			
Rotor–Stator Eq. (2.13)	✓	✓	✓			✓	✓	✓	✓			
Rotor–Stator Swirl Eq. (2.14)						✓	✓	✓	✓			

Since the correlations depend on Re and sometimes Pr, some fluid properties need to be extracted. They are extracted from the CFD simulation at the position of the nodes in the FEA fluid network. Specifically, it is the nodes that are connected to the thermal zones which are used for retrieving this fluid data. These points are illustrated as the black dots in Fig. 3.8; the thermal zones from Fig 3.4 are also illustrated here. The dashed boxes are not the actual zones, but rather just an illustration of where on the inside solid surface each zone boundary is.

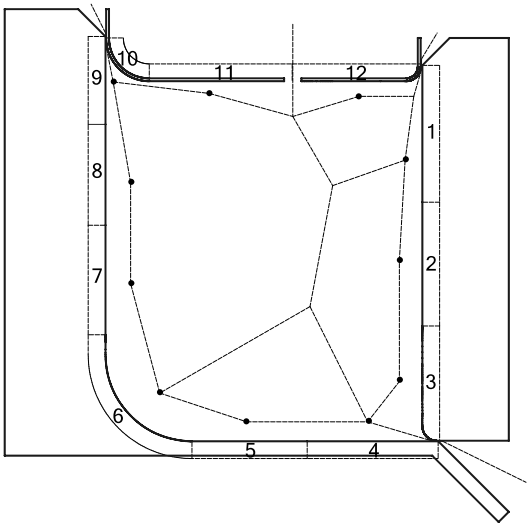

Figure 3.8: Location of the fluid nodes and their connected thermal zone.

Boundary Conditions

The outer boundaries get the same boundary condition as per T1–T6 in the CFD simulation, see Table 3.3. The first node of the inlet on the fluid network gets the same temperature and mass flow as the inlet (A) in the CFD model. Each element in the fluid network is assigned a mass flow according to Fig. 3.6. The zones in Fig. 3.4 each get a convective boundary condition connected to a fluid node with an HTC from the correlations, see App. F. The connected fluid node is the one closest to the middle of each thermal zone, illustrated previously in Fig. 3.8.

Table 3.6: Optimal correlation combination tested.

	Zone 1	Zone 2	Zone 3	Zone 4	Zone 5	Zone 6	Zone 7	Zone 8	Zone 9	Zone 10	Zone 11	Zone 12
Flat Plate Eq. (2.9)										✓	✓	✓
Rotating Disc Eq. (2.10)												
Rotating Cylinder Eq. (2.11)				✓	✓	✓						
Turbine Disc Eq. (2.12)	✓	✓	✓									
Rotor–Stator Eq. (2.13)							✓	✓	✓			
Rotor–Stator Swirl Eq. (2.14)						✓						

Since not all correlations are valid everywhere, there will be different combinations of correlations for different thermal zones and cavity regions. Only the vertical parts of the two rotating discs are evaluated with different correlations, but they always use the same correlation for the entire wall. The five different correlation combinations are available in App. B. An optimal correlation combination is also

tested, combining the correlations that provided the best matching temperature between CFD and FEA, for each region, see Table 3.6.

Internal Heat Generation

To calculate the internal heat generation from the viscous sub-layer to the fluid, Eq. (2.17) is used. The equation introduces two unknowns required to obtain the internal heat generation from viscous work in the viscous sub-layer. Firstly, a velocity gradient away from the wall is needed, and secondly, a volume of the heat generation region is needed since viscous dissipation is defined as work per volume.

The velocity gradient is calculated using a linear approximation which is valid in the viscous sub-layer; see Eq. (2.21). Since the viscous sub-layer ends at $y^+ = 5$, the thickness of the viscous sub-layer is calculated as y from Eq. (2.19). From Eqs. (2.18) and (2.21), the velocity at this thickness away from the wall can be calculated, once again using that $y^+ = 5$. Since these equations assume a stationary wall, the velocity calculated is the same as the velocity difference between the wall and the end of the viscous sub-layer, which gives the linear velocity gradient from the wall. The calculation requires the friction velocity (u_τ), which is extracted from the CFD simulation using the area-averaged wall shear stress, which is used to calculate the friction velocity, see Eq. (2.20), for each thermal zone.

With the viscous dissipation calculated, the volume for the internal friction is set to the volume of the viscous sub-layer, since heat generation is applied to the fluid nodes connected to the thermal zones. Using the geometry information extracted with the Python script explained earlier, the area for each zone is calculated. Multiplying this area by the thickness of the viscous sub-layer gives an estimate of the sub-layer volume.

With the viscous dissipation and the volume of the viscous sub-layer, multiplying them together returns the heat generation from viscous work in the viscous sub-layer for one thermal zone. In ANSYS Mechanical, this is then added as Heat Flow to the connected fluid nodes. All correlation combinations are run both with and without the effect of viscous sub-layer internal friction included; the optimal correlation is only made for the case with friction included.

3.2.2 Post-processing

Other than temperature contours, 20 measurement probes are placed throughout the domain, as illustrated in Fig. 3.9. Ten of them are placed in the solids, spread out to capture the entire domain and mimicking experimental temperature extraction, and the other ten in the closest fluid node. Circles represent fluid probes and squares represent solid probes. They are numbered from the top of the LPT in a clockwise fashion. Here, the temperature is compared between the different correlations and the CFD simulation.

For the thermal zones in Fig. 3.4, the HTC value is compared between the different correlations and CFD. Here, the bulk fluid temperature is taken as the CFD temperature in the fluid node point connected to the thermal zone, the previously shown dots in Fig. 3.8. Finally, a comparison is made between the optimal correlation combination and the CFD solid temperatures by looking at contours of the delta between the two.

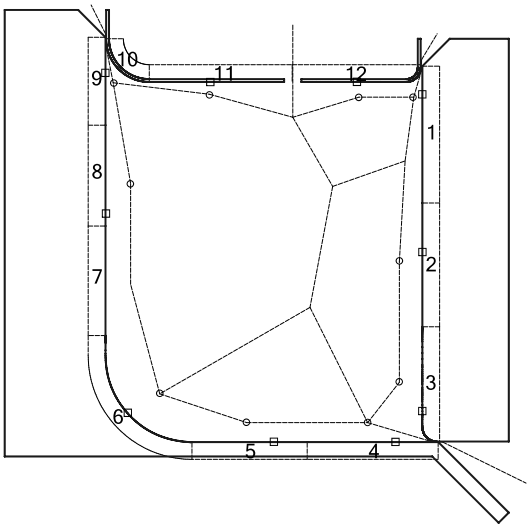

Figure 3.9: Probe positions for temperature readings, square for solid positions and circle for fluid positions, zones are marked as numbered boxes.

4

Results

This chapter will present the results from the CFD simulations and correlation-based FEA model, along with a comparison between the two. In chapter 5, further discussion of these results will be made, connecting back to the theory.

4.1 Computational Fluid Dynamics

The distribution of mass flow used in the FEA model to design the fluid network from Fig. 3.6 is seen in Fig. 4.1. The flow direction of the fluid is indicated by the arrows. This highlights three recirculation regions: one from the inlet along the HPT and two going up the LPT. The left recirculation region has the majority of the mass flow.

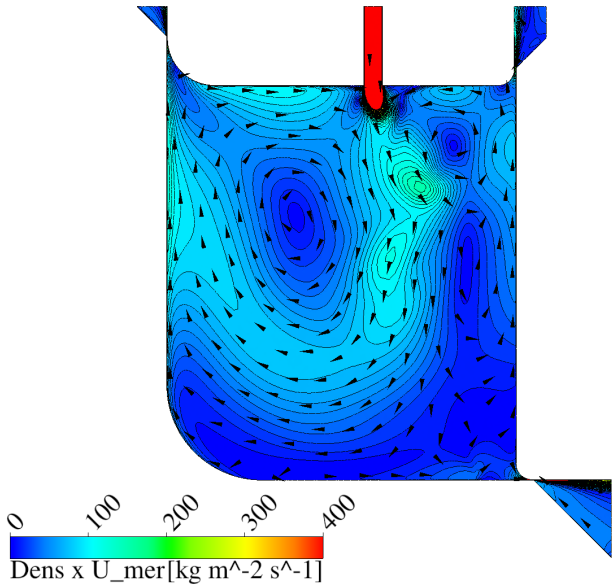

Figure 4.1: Distribution of mass flow, see Eq. (2.24), along with fluid flow direction.

Figure 4.2 shows the surfaces used to create the mass flow distribution in the FEA model according to Sec. 3.2.1. The underlying CFD mass flow distribution is also seen. The surfaces are curved with the sector cavity and mainly placed where the recirculation regions meet the walls. The surface at the bottom of the HPT is sized

and positioned to try to ensure all flow is in the same direction as the fluid element in Fig. 3.6, i.e. rightward in the figure. Integrating the mass flow over these surfaces and then area-averaging returns the mass flow passing through the surface. This is used to define the mass flow for the wall-related fluid elements in the FEA model, which is then used to calculate the bulk fluid temperature in the convective equation; see Eq. (2.2).

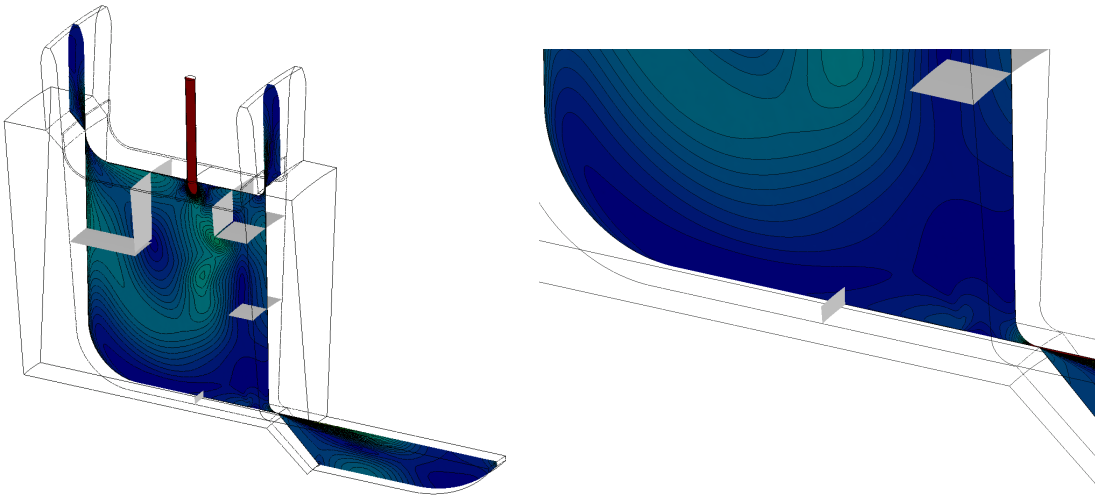

Figure 4.2: Surfaces (grey) used to evaluate the mass flow in the FEA fluid elements, with close-up on bottom (right).

The swirl in the cavity depends only on the tangential velocity; this is presented in Fig. 4.3. The tangential velocity is, in general, the dominant velocity direction. The tangential velocity increases away from the inlet, and it is seen that the inlet slows down the rotation of the fluid.

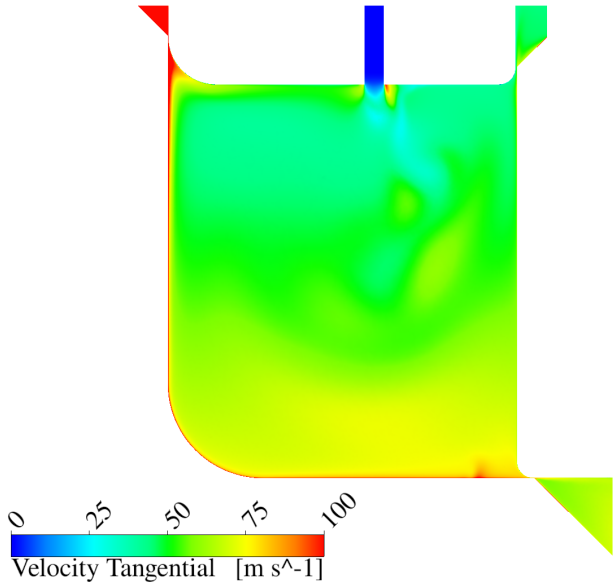

Figure 4.3: Contours of the tangential velocity in the fluid.

With the tangential velocity, the swirl ratio, from Eq. (2.8), is calculated, and contours of this are seen in Fig. 4.4. It is presented in the stationary frame of reference against the rotation of the HPT as Ω. In general, it shows a gradient from a lower ratio at the top of the cavity and increasing as it reaches the bottom of the cavity, with perturbations from the radial inlet flow.

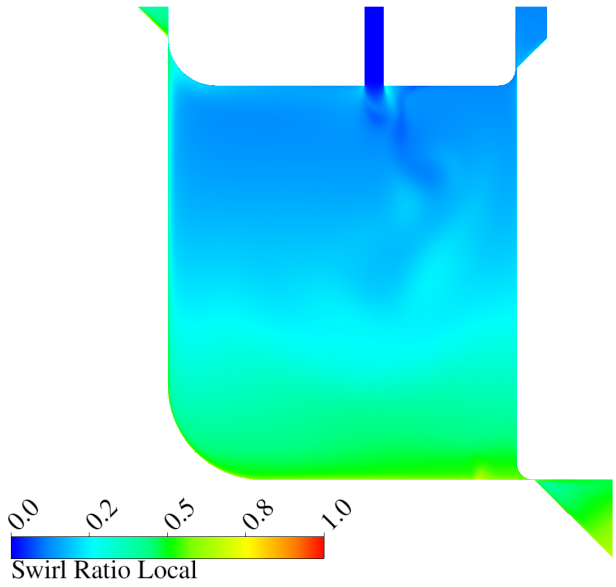

Figure 4.4: Contours of the swirl ratio in the fluid.

Figure 4.5 shows the swirl ratio along three lines through the fluid with normalized axial distance; their location is seen in Fig. 3.5. It is seen again that the swirl ratio increases away from the inlet. This more clearly shows how the swirl ratio quickly stabilizes away from the HPT before reaching the inlet and finally the LPT disc.

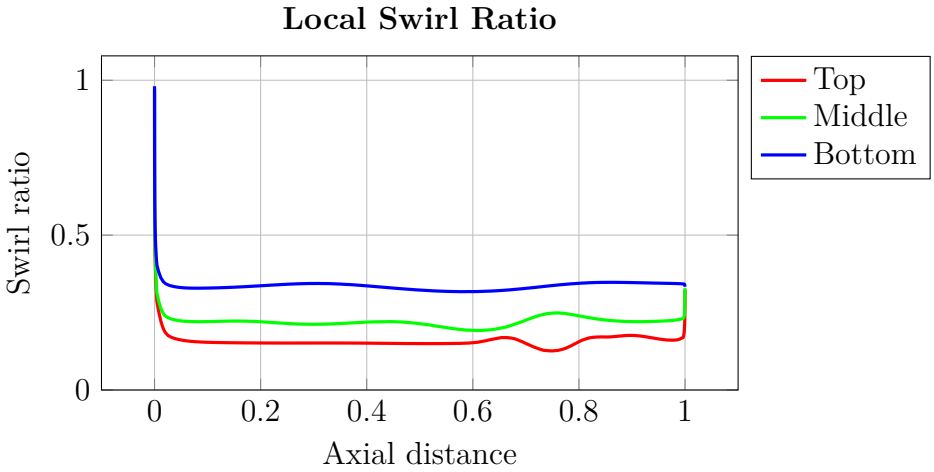

Figure 4.5: Swirl ratio along three lines in the fluid, normalized x-axis.

The temperature of the solids and fluid from the CFD simulation can be seen in Fig. 4.6. The temperature gradient in the solids from the linear boundary conditions can be observed. This range of temperature of the colour bar from 500 K to

900 K is due to the exterior wall boundary condition applied to the HPT. The fluid temperature is relatively constant, with only a warmer region near the inlet and cooler at the bottom close to seal clearance D, see Fig. 3.1, at the bottom right of the domain. This is hard to see as a result of the more interesting solid temperature varying so much. The outlet temperature also varies in relation to each other and the inside of the cavity.

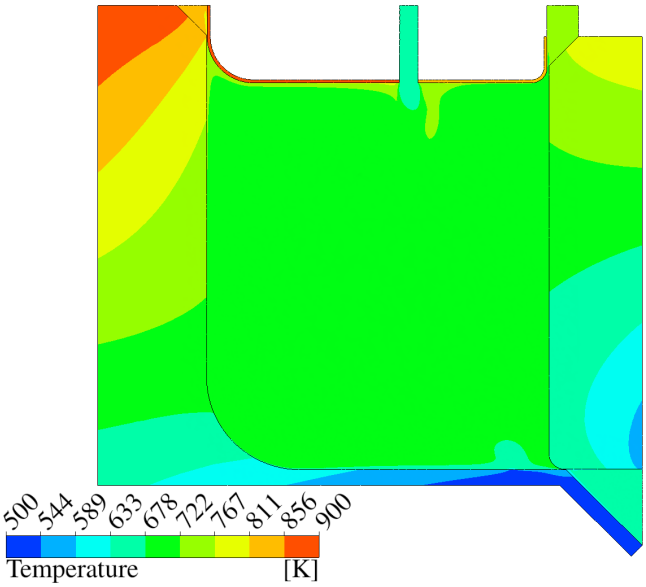

Figure 4.6: Contours of the temperature in the domain.

4.1.1 Additional Cases

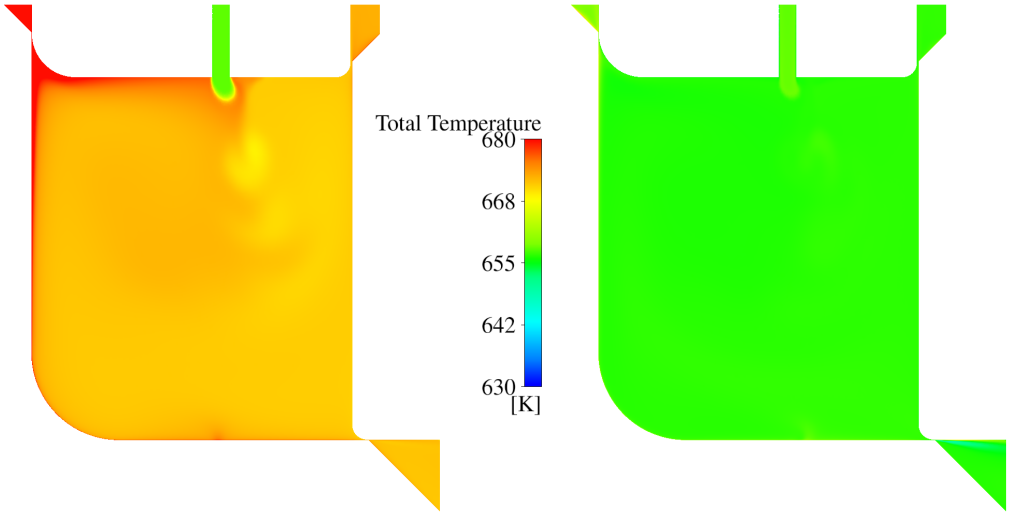

Figure 4.7: Total temperature contours for the case with friction (left) and without (right).

For the cases with viscous work, or friction, enabled and disabled, the total temperature ($T_{\text{static}} + u^2/(2c_p)$) contours are presented in Fig. 4.7. The most obvious is the

heating caused by internal, irreversible friction, seen by the significantly higher temperature compared to the no-friction case. Another difference is the local changes in total temperature when frictional effects are included, whereas the non-friction case is relatively constant.

The total temperature is also presented along the same three lines as the swirl ratio, see Fig. 4.8. Obvious for both cases is the distinct increase in total temperature close to the HPT, and to some degree, the LPT as well. What is most interesting, and useful for the rest of the project, is that the total temperature increases by ≈15 K when viscous work is included in the model.

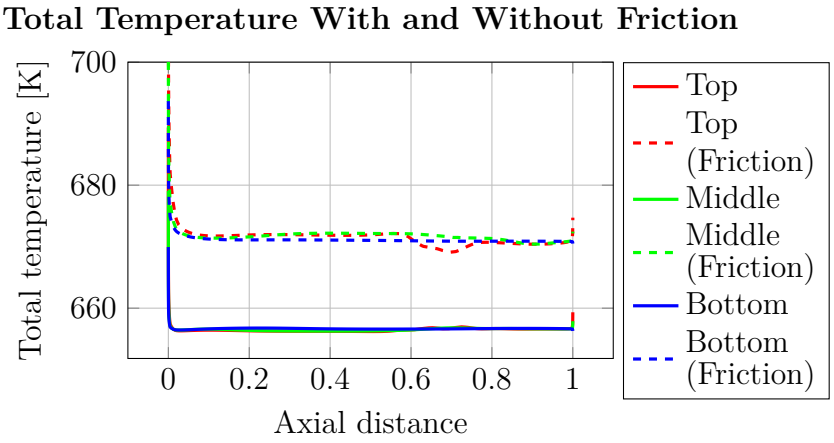

Figure 4.8: Total temperature along three lines with and without viscous work.

4.1.2 Model Validation

Figure 4.9 shows the relation between meshes with different y^+ values and the HTC, with a bulk fluid temperature as the volume average in the middle of the cavity used. The change between refinement levels decreases drastically as y^+ is within the viscous sub-layer. It is presented for four thermal zones, from Fig. 3.4, which remain similar in behaviour between meshes, i.e. there is no change in direction for the flux or aggressive gradients in them. After the maximum y^+ is around one, the change in HTC has subsided.

To better gauge how much the value changes between y^+ meshes, the percentage difference between them is presented in Table 4.1. This clearly shows that after a mesh with a y^+ value of around one, there is little change in the HTC. All results were presented for this mesh.

Table 4.1: Change in HTC [$\mathrm{W\,m^{-2}\,K^{-1}}$] between refinement levels, in percent.

y^+	**Zone 1**	**Zone 4**	**Zone 9**	**Zone 11**
$10 \rightarrow 3$	32.0	19.0	22.4	16.3
$3 \rightarrow 1$	7.1	6.9	4.9	11.4
$1 \rightarrow 0.5$	5.2	4.4	3.2	0.61

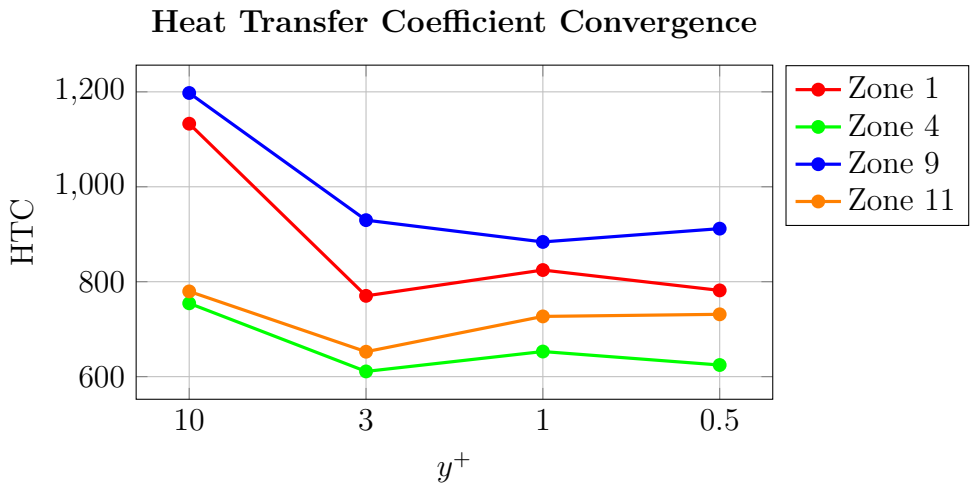

Figure 4.9: HTC [$\mathrm{W\,m^{-2}\,K^{-1}}$] at different stations for different y^+ values.

The resolution of the boundary layer is presented in Fig. 4.10. It is presented for both the HPT and LPT from the wall until the velocity becomes zero. Both the velocity and normal distance are normalized, and the cell centres are marked. A smooth development of the wall tangential velocity is seen, especially in the high-gradient area close to the wall.

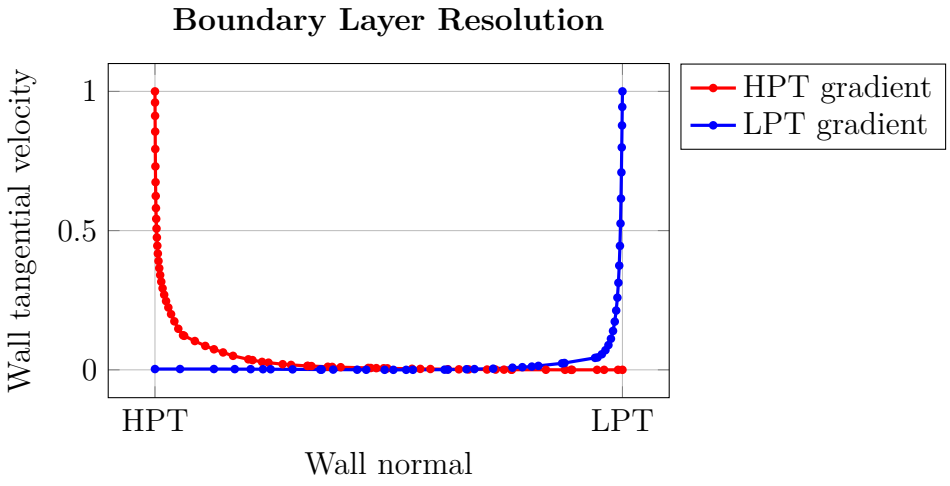

Figure 4.10: Wall tangential fluid velocity along the wall normal direction, both normalized with the maximum.

For the validation of changing the solid temperature and evaluating the HTC, the different HTC values are presented in Table 4.2. The percentage difference from the original case is presented in Table 4.3. Overall, the change in HTC is small, and the model is acceptable considering the other validations made. The model validation utilized slightly different temperature boundary conditions for T3 and T4.

Table 4.2: HTC [$\mathrm{W\,m^{-2}\,K^{-1}}$] for the cases with different temperature.

Case	Zone 1	Zone 4	Zone 9	Zone 11
+25 K	808.6	627.5	929.7	751.9
Reference	824.6	652.9	883.8	726.9
−25 K	868.5	641.6	833.4	760.0

Table 4.3: Percentage change for HTC [$\mathrm{W\,m^{-2}\,K^{-1}}$] to the original case.

Case	Zone 1	Zone 4	Zone 9	Zone 11
+25 K	1.9	3.9	5.2	3.4
−25 K	5.3	1.7	5.7	4.6

4.2 Finite Element Analysis

Figure 4.11 shows the temperature distribution from the FEA model using the optimal correlation combination. The outside wall temperature gradient from the boundary conditions is seen. On the inside walls of the cavity, the temperature is skewed towards the seal clearances. The fluid elements inside the cavity have an overall conforming temperature, differing mainly at the inlet and near the bottom of the HPT.

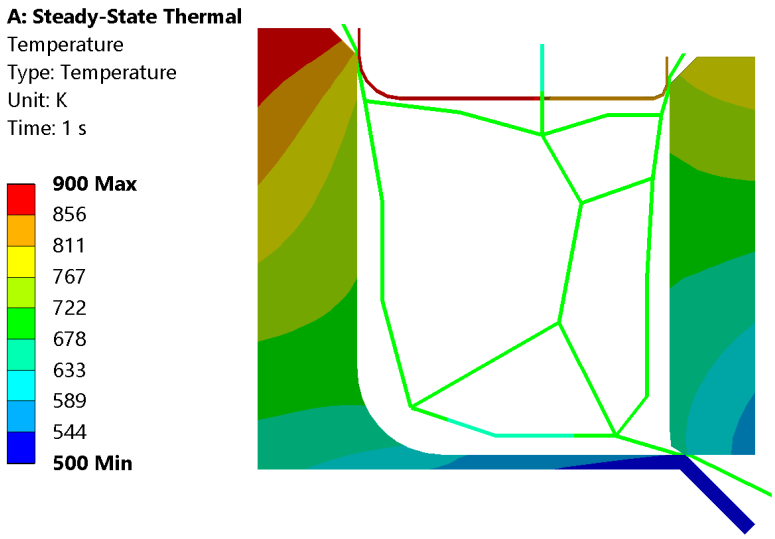

Figure 4.11: Temperature contours for the optimal correlation combination.

To validate the correlation-based model against CFD fluid and solid probes from Fig. 3.9 are used, one on each side of the cavity near the seal clearances. The difference between the correlation-based model and CFD temperature, FEA − CFD, is presented for a selection of probe points; in Table 4.4 without the internal frictional heating implemented, and in Table 4.5 with the friction implemented. The cells are coloured depending on how large the difference is from CFD. Green cells are within

14 K, orange and light blue cells from 14 K to 28 K, and blue cells above 28 K. The range for green cells is considered a good match in this project. Without friction, the FEA model generally underpredicts the temperature, especially in the fluid. For the solid temperatures, which are the most important, the majority are close to the CFD, with Solid 8 being significantly colder.

Table 4.4: Difference between the correlation combinations in App. B and CFD temperature [K].

Probe	C1	C2	C3	C4	C5
Solid 1	4.2	−1.0	−6.7	−1.0	−0.7
Solid 4	−12.1	−0.9	−0.7	−0.9	−0.7
Solid 8	21.0	−61.1	−28.2	−28.0	−37.2
Solid 9	2.0	2.1	2.1	2.1	2.1
Fluid 1	−21.0	−18.2	−19.9	−21.0	−20.2
Fluid 4	−1.7	−0.6	0.4	−0.6	0.2
Fluid 8	−32.6	−28.7	−27.4	−28.7	−27.7
Fluid 9	−25.4	−18.4	−20.2	−21.5	−20.4

With friction implemented in the FEA model, the temperature increases compared to CFD. Thus, the fluid temperatures are, in general, much closer than before. However, the increase in temperature means that some correlations and probe points are now too warm instead. Solid 8 is, in general, too cold both with and without friction, of course, less so with friction. The full temperature data is available in a visualization in App. C and in raw format in App. D.

Table 4.5: Difference between the correlation combinations in App. B with internal frictional heating implemented and CFD temperature [K].

Probe	C1	C2	C3	C4	C5	Opt
Solid 1	9.7	5.5	1.0	5.5	5.8	0.7
Solid 4	−9.8	2.4	2.6	2.4	2.6	2.4
Solid 8	28.0	−45.3	−15.5	−15.4	−23.6	−15.3
Solid 9	2.4	2.5	2.5	2.5	2.5	2.5
Fluid 1	−6.1	−4.5	−3.8	−4.5	−3.8	−4.4
Fluid 4	15.9	15.7	16.5	15.7	16.5	15.8
Fluid 8	−11.5	−8.7	−7.8	−8.7	−7.7	−8.5
Fluid 9	−4.3	−1.6	−0.6	−1.6	−0.6	−1.4

The difference between the CFD simulation temperature and the optimal correlation combination, from Table 3.6, is presented in Fig. 4.12. Thus, it presents the difference between the solid temperature in Figs. 4.6 and 4.11. A delta to the CFD model larger than 14 K is coloured grey. Overall, the difference between FEA and CFD is very small, with the FEA model tending towards the colder side. Inside the cavity, there is a hotspot around the inlet with a larger cold spot towards the top of the HPT and a smaller one towards the bottom; the top of the HPT is also where Solid 8 from Table 4.5 is located. After the seal clearances, the temperature

generally differs more between the CFD and FEA, with the bottom clearance even affecting the inside of the cavity slightly.

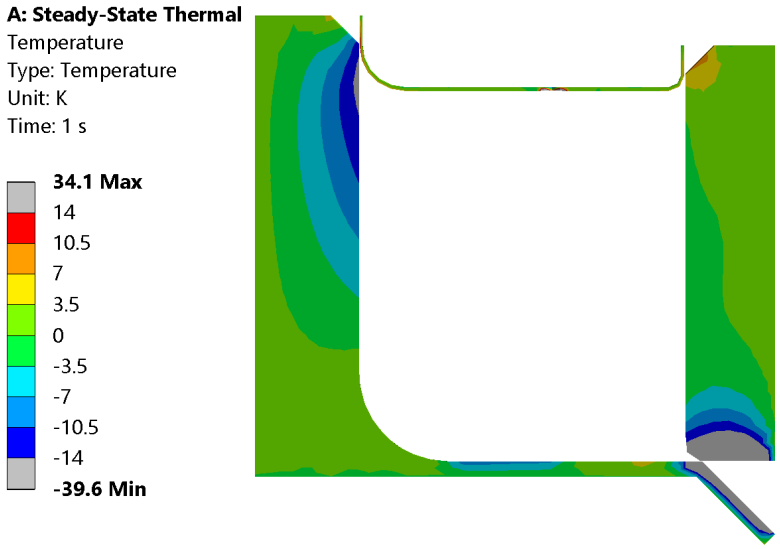

Figure 4.12: Temperature delta between CFD and optimal FEA simulation.

4.2.1 Internal Heat Generation

The effect of viscous work, for a selection of zones from Fig. 3.4, is presented in Table 4.6. It is seen that at the top of the domain, where the discs' tangential velocity is higher, it also generates more internal heat from friction. The HPT, which has the highest rotational velocity, is responsible for the majority of the heat generation. The effect of viscous work for all zones is presented in App. E.

Table 4.6: Friction velocity (u_τ) and heat generation added to the FEA model.

Thermal Zone	Friction Velocity [m/s]	Heat Generation [W]
Zone 1	3.3	7.1
Zone 4	3.1	1.7
Zone 9	10.9	174.0
Zone 11	3.8	9.2

4.2.2 Heat Transfer Coefficient

A selection of the HTC values calculated from the CFD and different correlations, along with the percentage difference between them, is presented in Table 4.7 for their respective thermal zones from Fig. 3.4. Unlike the temperatures presented previously, the HTC value differs significantly more from the CFD simulation. Combination 1, which consists of the flat plate correlation, underpredicts the HTC value. The combinations with rotational correlations (C2–C5) generally underpredict the HTC value on the LPT and overpredict it for the vertical part of the HPT. It is seen

that the cylindrical correlation used along the bottom of the HPT (Zone 4) is close to CFD. Furthermore, the rotational correlations overpredict the HTC at the top of the HPT by around 30% to 90%. HTC values for all zones are available in App F. The fluid bulk temperatures used to calculate the HTC from the CFD simulation, along with the coordinates of where they were extracted, are available in App. G.

Table 4.7: HTC [$\mathrm{W\,m^{-2}\,K^{-1}}$] from CFD and the different correlation combinations, see App. B.

Thermal Zone	**CFD**	**C1**	**C2**	**C3**	**C4**	**C5**	**Opt**
Zone 1	788.8	385.8	558.4	783.8	557.8	557.8	783.8
Zone 1 Δ%		−51.1	−29.2	−0.6	−29.3	−29.3	−0.6
Zone 4	809.3	487.5	780.4	780.4	780.4	780.4	780.4
Zone 4 Δ%		−39.8	−3.6	−3.6	−3.6	−3.6	−3.6
Zone 9	1058.6	433.5	1415.5	1983.0	1411.2	1790.9	1411.2
Zone 9 Δ%		−59.0	33.7	87.3	33.3	69.2	33.3
Zone 11	774.6	458.8	458.8	458.8	458.8	458.8	458.8
Zone 11 Δ%		−40.8	−40.8	−40.8	−40.8	−40.8	−40.8

The Re_Ω numbers used to calculate the HTC from the correlations using Eqs. (2.10)–(2.14) are presented in Table 4.8. Re ranges from 6.37×10^5 to 7.14×10^6 with the lowest at the bottom of the slow-rotating LPT and the highest at the top of the faster HPT, which is outside the validated range for the correlations. The highest validated Re_Ω is 1.2×10^6 for the turbine disc in Sec. 2.4.4.

Table 4.8: Re_Ω for the rotating thermal zones.

Zone	$\boldsymbol{Re}$
Zone 1	2.04×10^6
Zone 2	1.21×10^6
Zone 3	6.37×10^5
Zone 4	1.35×10^6
Zone 5	1.31×10^6
Zone 6	1.72×10^6
Zone 7	3.38×10^6
Zone 8	5.25×10^6
Zone 9	7.14×10^6

5

Discussion

This chapter will discuss the results from both the CFD simulations and the FEA simulations, along with a comparison between the two.

5.1 Computational Fluid Dynamics

From Fig. 4.6, the larger variation in the temperature after the seal clearances compared to the rest of the fluid is a result of higher heat transfer between the solids and fluid at these clearances. As the fluid passes through the seal clearance, its velocity increases, reducing the thickness of the thermal boundary layer. This leads to the HTC increasing in this region, causing greater flux to or from the fluid. This explains both the change in fluid temperature and the solid temperature skewness towards the seal clearances. This is especially obvious after the top left seal clearance (B).

Similarly, the small region of slightly cooler fluid near seal clearance D can be explained by this. Looking at Figs. 4.1 and 4.5, the impingement of the fluid separating from the large HPT recirculation causes an increase in heat flux between the bottom of the HPT and the fluid. In this case, the fluid is cooled by the solid, whereas at outlet B it is heated.

When it comes to swirl in the cavity, a few things should be noted. Firstly, looking at Fig. 4.5, the Batchelor flow model appears accurate for this cavity, as expected, with a swirl ratio that remains largely constant throughout the middle of the cavity. However, there are some differences, mainly that the completely radial flow of the inlet slows down the rotation of the fluid in the cavity. As such, there will be a greater relative velocity between the fluid and solid and thus increased heat transfer between the two. Secondly, Fig. 4.7 and 4.8 shows a lot of tangential work on the fluid, increasing the total temperature near the wall. Whilst both cases utilize a high rotational rate on the discs, with viscous work enabled in the model, this tangential work and mixing at the inlet heat the fluid further.

The interaction between the swirling core and radial inlet logically causes a drop in the local swirl ratio. The tangential velocity decreases at the top of the domain and even more where it first mixes with the radial inlet, causing this reduction in swirl.

When viscous work is enabled in Fig. 4.8, the overall higher temperature means the inlet interaction can be seen as a local decrease in total temperature when the now colder inlet mixes with the warmer core.

5.1.1 Model Validation

The method used to obtain the CFD results is, with consideration of the limitations, robust. The y^+ study, see Sec. 3.1.2, saw that the mesh is of adequate resolution considering the chosen turbulence model and simulation type; see Fig. 4.9. Ideally, a finer mesh, using hexahedral elements, would be preferred for accuracy and computational efficiency, but it is not possible within the scope of the project. Likewise, a study into the choice of turbulence model was omitted from the thesis. Using anisotropic models to better evaluate the non-uniform turbulence near the walls, whilst beneficial for accuracy, increases complexity for the simulation.

Changing the temperature on the outer walls to test the validity of the model, whilst theoretically valid, is less reliable due to the complexity of this model. With three outlets, the added or subtracted energy from the change in outside wall temperature affects the flow field. At large temperature changes, the global flow would likely change. For small changes, the difference might not be clear, but the added energy to the kinematic boundary layer is expected to influence it through the change in fluid properties.

5.2 Finite Element Analysis

The CFD and correlation-based FEA models show similar behaviour, skewing the temperature field towards the clearances. The difference in temperature, seen in Fig. 4.12, between the CFD and FEA models in the diverging part after the clearances is explained by the implementation of boundary conditions. The CFD model has contact, and thus heat transfer, between the air and solid even after the clearance, whereas the FEA model does not. This is due to the inside of the cavity being the main focus and not the outlets.

The largest probed difference in temperature occurs at the top of the HPT, seen in Table 4.4 and 4.5. This is likely a result of the behaviour of the correlations and the fluid. Firstly, most of the correlations are only valid for a Re_Ω up to 10^6, whereas the HPT goes up to seven times this. Hence, the valid range of the correlations is greatly exceeded. On that note, it is interesting that the rotating cylinder correlation, Eq. (2.11), which was developed for low Reynolds in water, performs very well along the bottom of the HPT. That could mean the valid range is larger than that previously tested, or that the specific conditions in this case make it work.

The second reason behind the underprediction from the rotating correlations at the top of the HPT can be attributed to the shape of the cavity. Since the flow, for all intents and purposes, can not leave the cavity at the top of the HPT, its radial

velocity slows down, whereas a correlation allowing free flow out might assume a greater radial velocity. This would then result in a higher heat transfer between the solid and fluid. However, this same phenomenon was not evident for the LPT, either as a result of a larger outlet at the top of the disc or lower Re_Ω in general.

Regarding the stator, it is always very close to the CFD, staying well within the 14 K delta. Since it is so thin, the difference in temperature between the specified outside and the unspecified inside of the cavity will always be small. Thus, even with a large gradient, the short distance ensures that the treatment of the inside matters little regardless of simulation type or method. Even setting the temperature as constant, according to the boundary condition, would also yield an acceptable solid temperature. Of course, the fluid elements would have an increased temperature as a result.

Whilst the difference at the bottom of the HPT is small, the delta plot in Fig. 4.12 shows a colder region there. It is also the one place where the fluid temperature consistently became worse with friction implemented. This is due to two reasons. Firstly, the low mass flow means that inaccuracies in the HTC will affect the fluid more compared to other places where it more quickly evens out with other areas. Secondly, evaluating the mass flow itself is difficult as a result of the flow field there. The very thin rightward flow, along with the low mass flow in CFD, means it is more influenced by choices regarding the size and placement of the surface used to extract the CFD mass flow.

The implementation of internal friction in the FEA model proved especially necessary to predict more accurate fluid temperatures, except for Fluid 4, which instead became too warm. With the largest heat generation at the top of the HPT according to Table 4.6, the fluid field still remained relatively constant since it transports the heat within itself. The top of the HPT having the most heat generation is logical since the swirl ratio is lower, and thus the relative velocity between the disc and fluid is higher.

However, the model only implements the friction in the viscous sub-layer. Whilst this is the area of the flow with the largest velocity gradients, and thus more viscous work, it does ignore other important parts. These are mainly the internal friction in the outer region of the boundary layer and what is present in the recirculation regions. An area that is expected to have significant viscous dissipation is where the fully radial inlet flow meets the mostly tangential cavity flow. The problem arises with the need for the velocity gradient in this mixing region. Potentially, the gradient could be estimated by some relation between the rotation of the discs and mass flow from the inlet, but further studies into this subject are necessary.

5.2.1 Heat Transfer Coefficient

Whilst the temperature is the most critical result, the HTC in Table 4.7 should not be ignored completely. There is an observed behaviour between correlations and regions where the HTC is close to the CFD and an improved temperature estimate;

see Fig. 4.12. It is once again apparent that the HTC increases faster along the radius of the HPT from the correlations than from the CFD, which explains the cold region at the top of the HPT. With a higher HTC and colder fluid compared to the solid, the cooling effect on the solid is exaggerated. The same reasoning can be made for the other parts of the cavity as well. Since the fluid in general is colder than the solids, having a lower HTC compared to CFD results in less heat transfer to the fluid and thus warmer solid temperatures.

5.2.2 Correlations

The use of correlations to obtain a quicker estimation of solid temperature compared to full CHT simulations has proved useful. Below, a discussion regarding each correlation will be made. This discussion will be made from the cases where friction is enabled, as that has provided the best performance overall.

Whilst the flat plate correlation, see Eq. (2.9), is very general, the implementation of it is unreliable for this type of cavity and methodology. For example, the characteristic length should be from the beginning of the plate, but a continuous cavity has no real beginning. Each thermal zone has a beginning, but this is an inaccurate approximation and might explain a part of the error otherwise observed from the correlation.

The rotating disc correlation, seen in Eq. (2.10), is not the best at any one location, but still performs consistently. Compared to the other correlations, it is among the more accurate along the HPT. As it is for a free rotating disc, it is reasonable that it would have difficulties treating the complexity of the flow in the turbine cavity.

Following that, the turbine disc correlation in Eq. (2.12) saw better performance along the LPT and worse for the HPT. Thus, it better handled the flow at the LPT, which has a greater tangential velocity than the solid and thus an effectively larger than one swirl ratio. However, it performed the worst for the HPT, possibly as a result of the regular turbine disc cavity being one rotating disc enclosed by stationary walls. In that case, the swirl ratio would likely be lower, and thus a greater heat transfer between the two would take place, which is what the correlation predicted. It could also be that this correlation has the greatest difficulty in handling the high Reynolds flow.

For the regular rotor-stator correlation, see Eq. (2.13), the behaviour is very similar to that of the rotating disc. With the same exponent for Re as the rotating disc correlation, it just so happens that Pr in the rotating disc correlation makes the coefficient in the rotor-stator correlation almost the same. Adding the swirl ratio to this same correlation, as in Eq. (2.14), follows the same behaviour but is slightly worse, which is a result of the authors fitting the two correlations to the same data.

For the best performance using correlations, combining different correlations for different regions of the cavity, as was done in this project, is an option. This is difficult to do if no CFD has been performed, in which case the only optimization

would be for obvious situations such as a cylinder or disc region. The other option is, since they are all based on the same form of aRe_{Ω}^{b}, to select the coefficient and exponent depending on the problem at hand; this would likely yield the best results. However, it comes with the added cost of needing to perform CFD simulations to create the correlation. It is possible that the addition of the swirl ratio in the correlation could help it stay applicable for a wider range of problems since it has more knowledge of the fluid–solid relation. Similarly, inserting the swirl ratio in the turbine disc correlation, which now overshoots the HTC for the HPT, might bring it closer to reality.

For the correlations, looking into where or how the fluid properties are extracted from CFD is an important continuation. In this thesis, no consideration was made for the placement of the fluid nodes, and thus the probe location for fluid properties in the CFD. Since the HTC depends on variables from CFD, the accuracy of the model depends somewhat on where or how they are extracted. Likewise, the HTC calculated, not from correlations, but directly using the temperatures in CFD, depends on the bulk fluid temperature used. A better estimation of this bulk fluid temperature could possibly lead to a better match between CFD HTC and correlation HTC. Using some volume-averaged properties might be more accurate, but it raises the question of what to include since the bulk fluid temperature, for example, should be outside the thermal boundary layer.

6

Conclusion

This thesis has looked into the use of correlations to apply convective boundary conditions inside FEA instead of running a full CHT CFD simulation to evaluate thermal loading. From this, the following can be concluded:

- A good estimation of the SAS temperatures can be made using a thermal-only FEA model.
- It relies heavily on a good estimation of the underlying fluid flow from CFD.
- The choice of correlation used is essential for the accuracy of the model.
- The implementation of internal frictional heating is important, especially for fluid element temperatures.
- The swirl-based correlation did not consistently outperform the non-swirl formulation; in several regions, the simpler correlation provided better agreement with the CFD.

To expand on the points above, the method of using a thermal-only FEA model to evaluate the behaviour of a SAS cavity showed promising results. How it relates to other cavities is unknown for this thesis, as is the accuracy when a CFD solution is not available to create the fluid network from. With the bottom of the HPT being hard to estimate even with a CFD solution, and also being where the FEA fluid temperature sees the greatest difference to CFD, the dependency of the FEA model on the estimation of mass flow is relevant to investigate. Similarly, how to best extract fluid properties from CFD is also worth investigating to better validate an FEA model against CFD.

The implementation of the internal friction of the viscous sub-layer shows promising results. It is relevant to include physical principles which are not included by default in the FEA solver. This includes the internal friction, which was included in this project, but also flow behaviour such as the swirl in the cavity. With the general overshoot of the HTC, using the swirl ratio as a damper on Re_Ω, and thus the HTC value, might allow already existing correlations to behave better or at least to more physically predict the coefficient. However, the base correlation in itself is most important for the accuracy of the model and an important part to study for

multiple different scenarios.

To answer the problem questions stated in Sec. 1.3, it is possible to achieve a correlation-based FEA model that produces accurate results compared to CFD. Furthermore, the swirl in the cavity acts as a damper on the rotor HTC by reducing the influence of Re_Ω in the correlation. Although its inclusion in this work did not yield significant improvements, it is theoretically expected to enhance the generality of the correlation by incorporating additional flow physics. Lastly, the implementation of the fluid internal friction from the viscous sub-layer in the FEA proved accurate for estimating the temperature rise in the fluid.

6.1 Future Work

A key aspect to investigate in future work is to create a tailor-made correlation on the form $a((1-\beta)Re_\Omega)^b$, which is a generalization of Eq. (2.14), and then evaluate how far from the original flow pattern it stays valid. Ideally, a correlation that allows for drastically different fluid flows and geometries would be created, but that requires the correlation to use more information from the fluid, making the implementation without CFD more difficult. In general, correlations are created for specific geometries since a rotating disc and a cylinder have significantly different flow behaviour.

Along these lines, further improvement to the model itself would be relevant, such as implementing more types of internal friction from further out in the boundary layer and recirculation regions. However, doing this without requiring many more CFD simulations to be run is difficult. Potentially, creating some correlation that takes the rotational rate of the discs and flow through the inlet into account should be investigated to that effect. The other option is to study correlations for calculating the skin friction coefficient, which can then be used to calculate the friction velocity for different simulation cases. The implementation of the radiative heat transfer effect in both the CFD and FEA models would also be beneficial for accuracy.

To save time, there is the potential to run two-dimensional CFD simulations for quicker mass flow estimation. Whilst the cavity in this thesis is not rotationally symmetric, if the difference is small, it might prove better than manual estimation of the flow field if no CFD is performed. It would, in any case, give a quick estimation before running time-costly three-dimensional simulations. Thus, investigating how close a two-dimensional simulation is to a three-dimensional one could provide time savings in the future.

Lastly, on a more product development note, the effect of angling the inlet to change the purpose of the fluid could be investigated. Using an angle with the core rotation, the internal heating would be reduced, but so would the relative velocity, and thus HTC, between the fluid and solids. Angling against the core rotation would increase the HTC instead, but could have undesirable effects such as added stress on components or excessive vibration.

Bibliography

[1] F. Whittle, "Improvements relating to the propulsion of aircraft and other vehicles," UK Patent GB347206A, Apr. 16, 1931.

[2] S. Farokhi, *Aircraft Propulsion: Cleaner, Leaner and Greener*, 3rd Ed., Hoboken, NJ: Wiley, 2022.

[3] P. R. N. Childs, *Rotating Flow*. Oxford, U.K.: Butterworth-Heinemann, 2011.

[4] D. Woelki, "1D Secondary Air System Modeling for Application in Engine Predesign and Multi-Fidelity," in *Deutscher Luft- und Raumfahrtkongress (DLRK)*, Stuttgart, Germany, 2024. DOI: 10.25967/610187.

[5] R. D. Soghe, B. Facchini, L. Innocenti, and M. Micio, "Analysis of Gas Turbine Rotating Cavities by a One-Dimensional Model," in *ASME Turbo Expo*, Orlando, FL, 2009, pp. 355–364. DOI: 10.1115/GT2009-59185.

[6] D. Hunt and Y. Yuan, "Modelling Conjugate Heat Transfer within a Gas Turbine Secondary Air System Using Thermo-Fluid System Simulation," in *ASME Turbo Expo*, 2020. DOI: 10.1115/GT2020-14202.

[7] *Heat flow fundamentals*, ANSYS Mechanical APDL Theory Reference, Release 2025 R1, ANSYS, Inc. [Online]. Available: https://ansyshelp.ansys.com/public/account/secured?returnurl=/Views/Secured/corp/v251/en/ans_thry/thy_heat1.html.

[8] F. P. Incropera, D. P. Dewitt, T. L. Bergman, and A. S. Lavine, *Incropera's Principles of Heat and Mass Transfer*, 8th Ed., Hoboken, NJ: Wiley, 2017.

[9] F. M. White and H. Xue, *Fluid Mechanics*, 9th Ed., New York, NY: McGraw Hill, 2021.

[10] Y. Cati, S. aus der Wiesche, and M. Düzgün, "Investigation of Convective Heat Transfer and Stability on a Rotating Disk: A Novel Experimental Method and Thermal Modeling," *Fluids*, vol. 9, no. 7, p. 167, 2024. DOI: 10.3390/fluids9070167.

[11] K. M. Becker, "Measurements of convective heat transfer from a horizontal cylinder rotating in a pool of water," Aktiebolaget Atomenergi, Stockholm, Sweden, Tech. Rep. AE-107, 1963. [Online]. Available: https://www.osti.gov/etdeweb/servlets/purl/20930974.

[12] G. Qureshi, M. H. Nguyen, N. R. Saad, and R. N. Tadros, "Heat Transfer Measurements for Rotating Turbine Discs," in *ASME Turbo Expo*, 1989. DOI: 10.1115/89-GT-236.

[13] R. P. Roy, G. Xu, and J. Feng, "A Study of Convective Heat Transfer in a Model Rotor–Stator Disk Cavity," *Journal of Turbomachinery*, vol. 123, no. 3, pp. 621–632, Jul. 2001. DOI: 10.1115/1.1371776.

[14] J. F. Wendt, J. D. Anderson, G. Degrez, E. Dick, and R. Grundmann, *Computational Fluid Dynamics: An Introduction*, 3rd Ed., Berlin, Germany: Springer, 2009.

[15] I. Newton, *Philosophiæ Naturalis Principia Mathematica*. London, U.K.: Royal Society, 1687.

[16] S. U. Nair and S. Somanath, *Introduction to Finite Element Analysis*. Singapore: Springer, 2024.

[17] L. Davidson, *Fluid Mechanics, Turbulent Flow and Turbulence Modeling*. Göteborg, Sweden, 2025, [Ebook]. Available: https://www.tfd.chalmers.se/~lada/postscript_files/solids-and-fluids_turbulent-flow_turbulence-modelling.pdf.

[18] A. Noori. "Conjugate Heat Transfer (CHT). "[Online]. Available: https://cfdland.com/conjugate-heat-transfer-cht/.

[19] *Fluid116—coupled thermal-fluid pipe*, ANSYS Mechanical APDL Theory Reference, Release 2025 R1, ANSYS, Inc. [Online]. Available: https://ansyshelp.ansys.com/public/account/secured?returnurl=/Views/Secured/corp/v251/en/ans_thry/thy_el116.html.

A

Code

Code A.1: Example of geometry extraction code.

```
from pycdb import read_cdb
import numpy as np


class ExtractGeometry():
    """Class to extract geometry from a .cdb file from Ansys.

    Extracts zone information in the form of node coordinates and what
    fluid nodes are connected to said zone.

    :param filename: Path to the Ansys .cdb file."""

    def __init__(self, filename:str):
        self.cdb = read_cdb(filename)

    @staticmethod
    def _expand_list(nodes:list):
        """Expands compressed lists from pycdb."""

        for i, node in enumerate(nodes):
                # List is compressed using negative values, e.g. 5 to 10
    is written 5, -10.
                if node < 0:
                    nodes[i] = np.abs(node)
                    nodes.extend(range(nodes[i-1]+1, np.abs(node)))
        return nodes

    def extract_zones(self, name_selection=r'^h100_\d+'):
        """Extracts zone information from .cdb files.

        Extracts zone naming, which nodes each zone connects to and the
        coordinates for said node. Returns information in nestled dicts.

        :param name_selection: Ansys named selection of zones, utilizing
    RegEx
```

```
            to find instances.

        :returns: A dict with zones as keys and dicts of nodes as values,
            the node dicts value is a list of coordinates [x, y, z].
        """

        thermal_zones = self.cdb.components.filter(name_selection)

        zone_mapping = {}
        for zone in thermal_zones:
            # Each zone is connected to the cell nodes in it.
            zone_mapping[zone.name] = {}
            nodes = zone.compressed_items

            # Check if list is compressed by checking for negative values in it.
            if any(node < 0 for node in nodes):
                nodes = self._expand_list(nodes)

            for node in nodes:
                # The relevant node coordinates are extracted from all nodes.
                node_coords = self.cdb.nodes[self.cdb.nodes.index==node][['x', 'y', 'z']]
                x = node_coords['x'].values[0]
                y = node_coords['y'].values[0]
                z = node_coords['z'].values[0]
                # Each cell node is connected to its coordinates.
                zone_mapping[zone.name][node] = [x, y, z]
        return zone_mapping
```

Code A.2: Example of correlation code.

```
from abc import ABC, abstractmethod
import numpy as np
from zone import Zone


# Registration for correlations using decorators
CORRELATION_REGISTRY = {}
def register(name:str):
    def decorator(cls):
        CORRELATION_REGISTRY[name] = cls
        return cls
    return decorator


class BaseCorrelation(ABC):
    """Correlation recipe."""

```

```
18      @abstractmethod
19      def compute_nusselt(self, zone:Zone):
20          """The individual correlation method."""
21          pass
22
23      @abstractmethod
24      def _char_len(self, zone:Zone):
25          # Characteristic length for Reynolds and HTC.
26          pass
27
28      def compute_htc(self, zone:Zone):
29          """Calculates HTC from the correlation.
30
31          :param zone: Zone object.
32
33          :returns: HTC for the correlation/zone.
34          """
35
36          htc = self.compute_nusselt(zone) * zone.k_f / self._char_len(zone)
37          return htc
38
39
40  @register('RotatingDisc')
41  class RotatingDisc(BaseCorrelation):
42      """Nusselt correlation for a rotating disc in quiescent fluid."""
43
44      def _char_len(self, zone:Zone):
45          # Characteristic length of the correlation, set as radius.
46          return np.mean(zone.r)
47
48      def compute_nusselt(self, zone:Zone):
49          """Nusselt correlation for a rotating disc."""
50
51          omega = zone.rpm * np.pi / 30
52          reynolds = omega * self._char_len(zone)**2 / zone.nu
53          prandtl = zone.nu / zone.alpha
54
55          K = 0.0186 * (0.6 + 2.6)**0.2 * prandtl**0.6
56          c_R = 0.8
57          return K * reynolds**c_R
```

B

Correlation Combinations

Table B.1: Combination 1 of correlations.

	Zone 1	Zone 2	Zone 3	Zone 4	Zone 5	Zone 6	Zone 7	Zone 8	Zone 9	Zone 10	Zone 11	Zone 12
Flat Plate Eq. (2.9)	✓	✓	✓	✓	✓	✓	✓	✓	✓	✓	✓	✓
Rotating Disc Eq. (2.10)												
Rotating Cylinder Eq. (2.11)												
Turbine Disc Eq. (2.12)												
Rotor–Stator Eq. (2.13)												
Rotor–Stator Swirl Eq. (2.14)												

Table B.2: Combination 2 of correlations.

	Zone 1	Zone 2	Zone 3	Zone 4	Zone 5	Zone 6	Zone 7	Zone 8	Zone 9	Zone 10	Zone 11	Zone 12
Flat Plate Eq. (2.9)										✓	✓	✓
Rotating Disc Eq. (2.10)	✓	✓	✓			✓	✓	✓	✓			
Rotating Cylinder Eq. (2.11)				✓	✓	✓						
Turbine Disc Eq. (2.12)												
Rotor–Stator Eq. (2.13)												
Rotor–Stator Swirl Eq. (2.14)												

Table B.3: Combination 3 of correlations.

	Zone 1	Zone 2	Zone 3	Zone 4	Zone 5	Zone 6	Zone 7	Zone 8	Zone 9	Zone 10	Zone 11	Zone 12
Flat Plate Eq. (2.9)										✓	✓	✓
Rotating Disc Eq. (2.10)												
Rotating Cylinder Eq. (2.11)				✓	✓	✓						
Turbine Disc Eq. (2.12)	✓	✓	✓			✓	✓	✓	✓			
Rotor–Stator Eq. (2.13)												
Rotor–Stator Swirl Eq. (2.14)												

Table B.4: Combination 4 of correlations.

	Zone 1	Zone 2	Zone 3	Zone 4	Zone 5	Zone 6	Zone 7	Zone 8	Zone 9	Zone 10	Zone 11	Zone 12
Flat Plate Eq. (2.9)										✓	✓	✓
Rotating Disc Eq. (2.10)												
Rotating Cylinder Eq. (2.11)				✓	✓	✓						
Turbine Disc Eq. (2.12)												
Rotor–Stator Eq. (2.13)	✓	✓	✓			✓	✓	✓	✓			
Rotor–Stator Swirl Eq. (2.14)												

Table B.5: Combination 5 of correlations.

	Zone 1	Zone 2	Zone 3	Zone 4	Zone 5	Zone 6	Zone 7	Zone 8	Zone 9	Zone 10	Zone 11	Zone 12
Flat Plate Eq. (2.9)										✓	✓	✓
Rotating Disc Eq. (2.10)												
Rotating Cylinder Eq. (2.11)				✓	✓	✓						
Turbine Disc Eq. (2.12)												
Rotor–Stator Eq. (2.13)	✓	✓	✓									
Rotor–Stator Swirl Eq. (2.14)						✓	✓	✓	✓			

C

Temperature Visualization

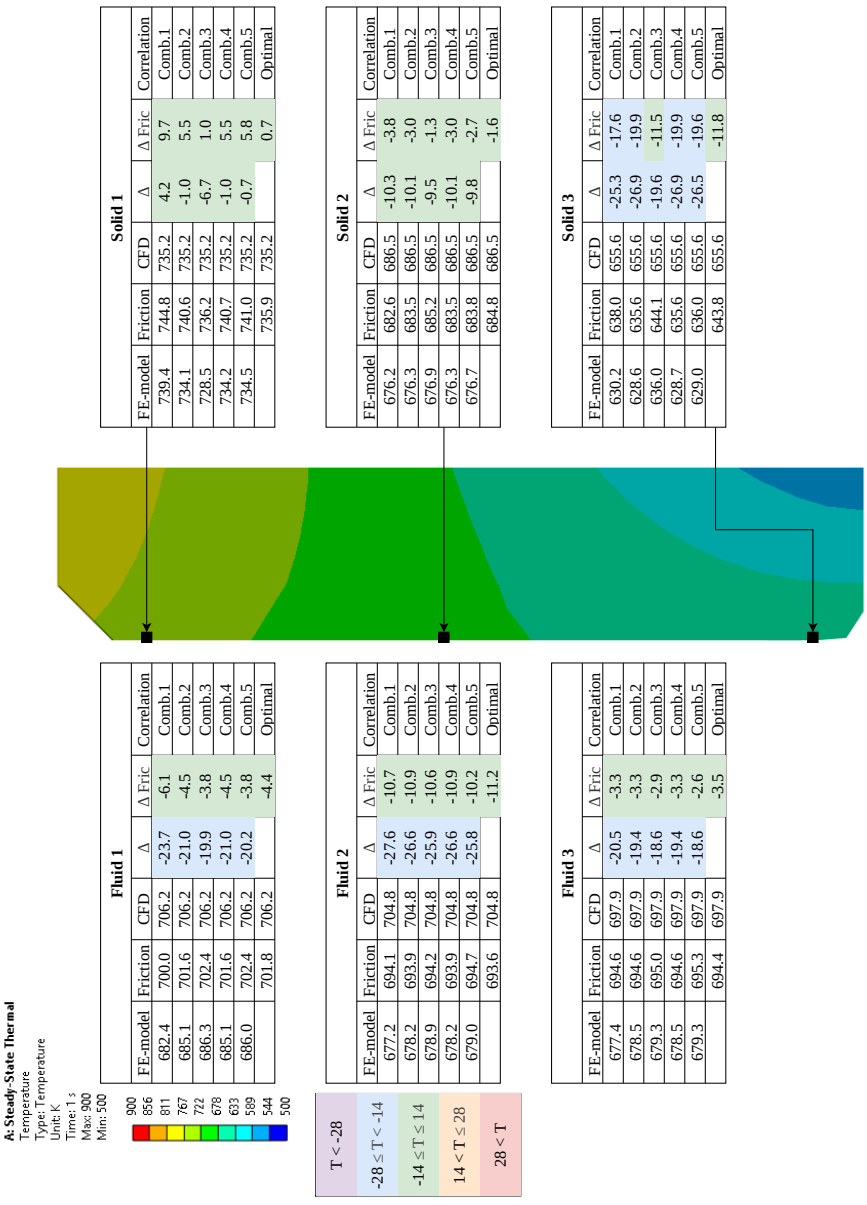

Figure C.1: Temperature probe point values for the LPT.

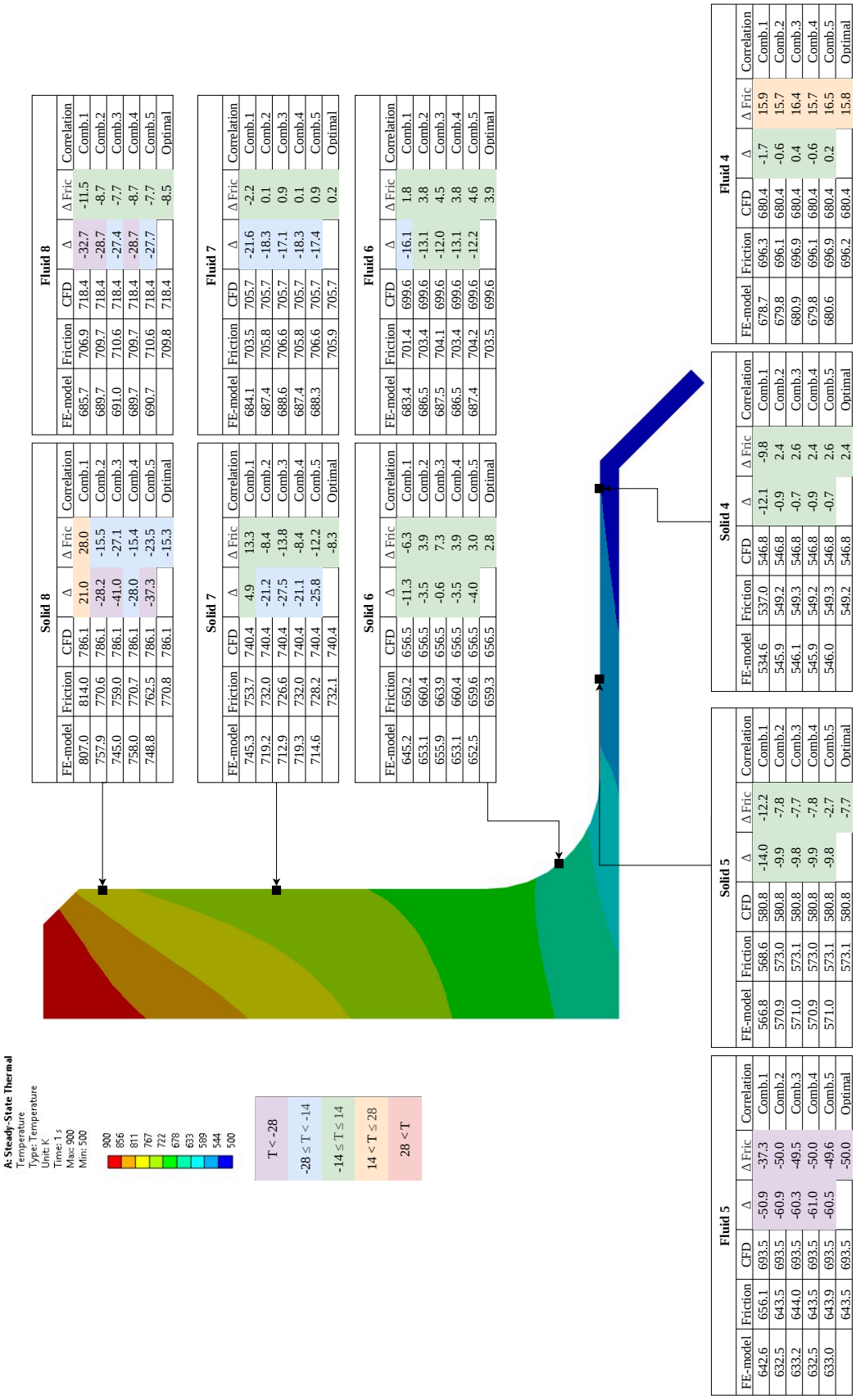

Solid 8

FE-model	Friction	CFD	Δ	Δ Fric	Correlation
807.0	814.0	786.1	21.0	28.0	Comb.1
757.9	770.6	786.1	-28.2	-15.5	Comb.2
745.0	759.0	786.1	-41.0	-27.1	Comb.3
758.0	770.7	786.1	-28.0	-15.4	Comb.4
748.8	762.5	786.1	-37.3	-23.5	Comb.5
	770.8	786.1		-15.3	Optimal

Fluid 8

FE-model	Friction	CFD	Δ	Δ Fric	Correlation
685.7	706.9	718.4	-32.7	-11.5	Comb.1
689.7	709.7	718.4	-28.7	-8.7	Comb.2
691.0	710.6	718.4	-27.4	-7.7	Comb.3
689.7	709.7	718.4	-28.7	-8.7	Comb.4
690.7	710.6	718.4	-27.7	-7.7	Comb.5
	709.8	718.4		-8.5	Optimal

Solid 7

FE-model	Friction	CFD	Δ	Δ Fric	Correlation
745.3	753.7	740.4	4.9	13.3	Comb.1
719.2	732.0	740.4	-21.2	-8.4	Comb.2
712.9	726.6	740.4	-27.5	-13.8	Comb.3
719.3	732.0	740.4	-21.1	-8.4	Comb.4
714.6	728.2	740.4	-25.8	-12.2	Comb.5
	732.1	740.4		-8.3	Optimal

Fluid 7

FE-model	Friction	CFD	Δ	Δ Fric	Correlation
684.1	703.5	705.7	-21.6	-2.2	Comb.1
687.4	705.8	705.7	-18.3	0.1	Comb.2
688.6	706.6	705.7	-17.1	0.9	Comb.3
687.4	705.8	705.7	-18.3	0.1	Comb.4
688.3	706.6	705.7	-17.4	0.9	Comb.5
	705.9	705.7		0.2	Optimal

Solid 6

FE-model	Friction	CFD	Δ	Δ Fric	Correlation
645.2	650.2	656.5	-11.3	-6.3	Comb.1
653.1	660.4	656.5	-3.5	3.9	Comb.2
655.9	663.9	656.5	-0.6	7.3	Comb.3
653.1	660.4	656.5	-3.5	3.9	Comb.4
652.5	659.6	656.5	-4.0	3.0	Comb.5
	659.3	656.5		2.8	Optimal

Fluid 6

FE-model	Friction	CFD	Δ	Δ Fric	Correlation
683.4	701.4	699.6	-16.1	1.8	Comb.1
686.5	703.4	699.6	-13.1	3.8	Comb.2
687.5	704.1	699.6	-12.0	4.5	Comb.3
686.5	703.4	699.6	-13.1	3.8	Comb.4
687.4	704.2	699.6	-12.2	4.6	Comb.5
	703.5	699.6		3.9	Optimal

Solid 5

FE-model	Friction	CFD	Δ	Δ Fric	Correlation
642.6	656.1	693.5	-50.9	-37.3	Comb.1
632.5	643.5	693.5	-60.9	-50.0	Comb.2
633.2	644.0	693.5	-60.3	-49.5	Comb.3
632.5	643.5	693.5	-61.0	-50.0	Comb.4
633.0	643.9	693.5	-60.5	-49.6	Comb.5
	643.5	693.5		-50.0	Optimal

Fluid 5

FE-model	Friction	CFD	Δ	Δ Fric	Correlation
566.8	568.6	580.8	-14.0	-12.2	Comb.1
570.9	573.0	580.8	-9.9	-7.8	Comb.2
571.0	573.1	580.8	-9.8	-7.7	Comb.3
570.9	573.0	580.8	-9.9	-7.8	Comb.4
571.0	573.1	580.8	-9.8	-2.7	Comb.5
	573.1	580.8		-7.7	Optimal

Solid 4

FE-model	Friction	CFD	Δ	Δ Fric	Correlation
534.6	537.0	546.8	-12.1	-9.8	Comb.1
545.9	549.2	546.8	-0.9	2.4	Comb.2
546.1	549.3	546.8	-0.7	2.6	Comb.3
545.9	549.2	546.8	-0.9	2.4	Comb.4
546.0	549.3	546.8	-0.7	2.6	Comb.5
	549.2	546.8		2.4	Optimal

Fluid 4

FE-model	Friction	CFD	Δ	Δ Fric	Correlation
678.7	696.3	680.4	-1.7	15.9	Comb.1
679.8	696.1	680.4	-0.6	15.7	Comb.2
680.9	696.9	680.4	0.4	16.4	Comb.3
679.8	696.1	680.4	-0.6	15.7	Comb.4
680.6	696.9	680.4	0.2	16.5	Comb.5
	696.2	680.4		15.8	Optimal

Figure C.2: Temperature probe point values for the HPT.

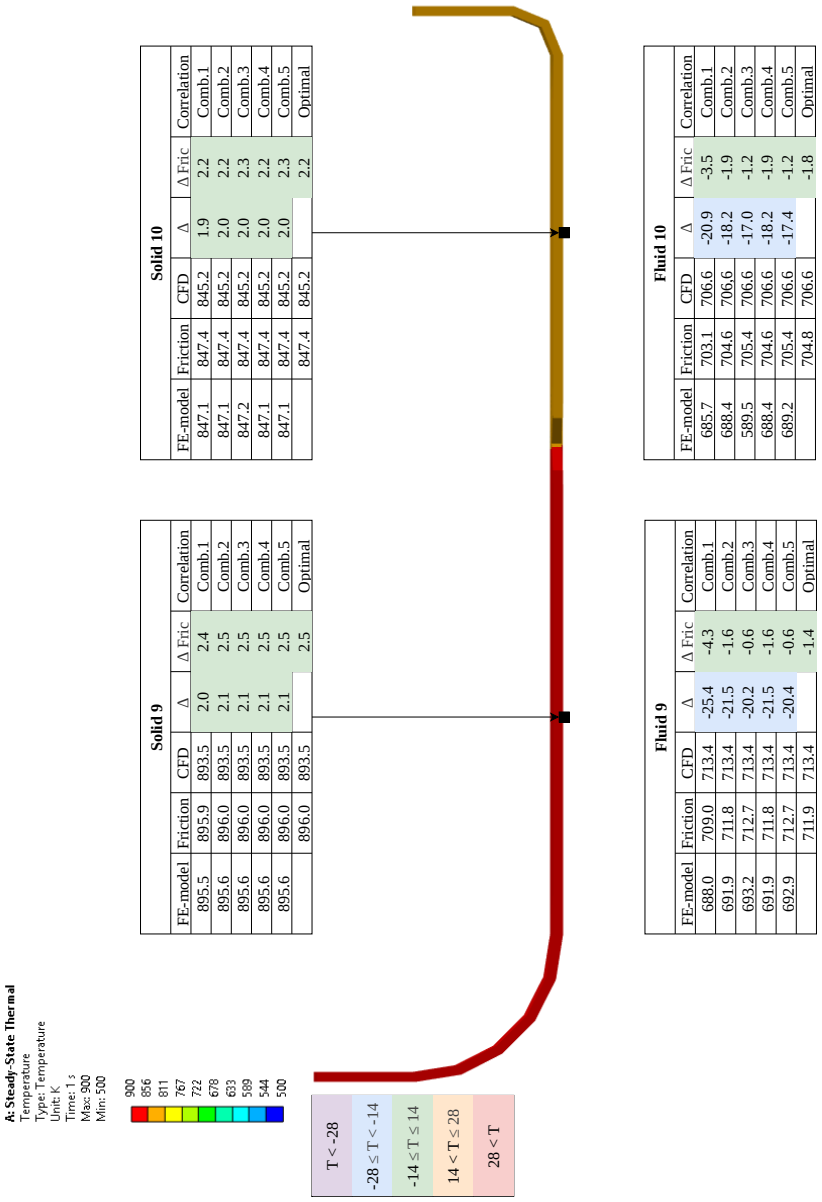

Solid 10

FE-model	Friction	CFD	Δ	Δ Fric	Correlation
847.1	847.4	845.2	1.9	2.2	Comb.1
847.1	847.4	845.2	2.0	2.2	Comb.2
847.2	847.4	845.2	2.0	2.3	Comb.3
847.1	847.4	845.2	2.0	2.2	Comb.4
847.1	847.4	845.2	2.0	2.3	Comb.5
	847.4	845.2		2.2	Optimal

Fluid 10

FE-model	Friction	CFD	Δ	Δ Fric	Correlation
685.7	703.1	706.6	-20.9	-3.5	Comb.1
688.4	704.6	706.6	-18.2	-1.9	Comb.2
589.5	705.4	706.6	-17.0	-1.2	Comb.3
688.4	704.6	706.6	-18.2	-1.9	Comb.4
689.2	705.4	706.6	-17.4	-1.2	Comb.5
	704.8	706.6		-1.8	Optimal

Solid 9

FE-model	Friction	CFD	Δ	Δ Fric	Correlation
895.5	895.9	893.5	2.0	2.4	Comb.1
895.6	896.0	893.5	2.1	2.5	Comb.2
895.6	896.0	893.5	2.1	2.5	Comb.3
895.6	896.0	893.5	2.1	2.5	Comb.4
895.6	896.0	893.5	2.1	2.5	Comb.5
	896.0	893.5		2.5	Optimal

Fluid 9

FE-model	Friction	CFD	Δ	Δ Fric	Correlation
688.0	709.0	713.4	-25.4	-4.3	Comb.1
691.9	711.8	713.4	-21.5	-1.6	Comb.2
693.2	712.7	713.4	-20.2	-0.6	Comb.3
691.9	711.8	713.4	-21.5	-1.6	Comb.4
692.9	712.7	713.4	-20.4	-0.6	Comb.5
	711.9	713.4		-1.4	Optimal

Figure C.3: Temperature probe point values for the stator.

D

Temperature Data

Table D.1: Temperature [K] data for all correlations at probes.

Probe	**CFD**	**C1**	**C2**	**C3**	**C4**	**C5**
Solid 1	735.2	739.4	734.1	728.5	734.2	734.5
Solid 2	686.5	676.2	676.3	676.9	676.3	676.7
Solid 3	655.6	630.2	628.6	636.0	628.7	629.0
Solid 4	546.8	534.6	545.9	546.1	545.9	546.0
Solid 5	580.8	566.8	570.9	571.0	570.9	571.0
Solid 6	656.5	645.2	653.1	655.9	653.1	652.5
Solid 7	740.4	745.3	719.2	712.9	719.3	714.6
Solid 8	786.1	807.0	757.9	745.0	758.0	748.8
Solid 9	893.5	895.5	895.6	895.6	895.6	895.6
Solid 10	845.2	847.1	847.1	847.2	847.1	847.1
Fluid 1	706.2	682.4	685.1	686.3	685.1	686.0
Fluid 2	704.8	677.2	678.2	678.9	678.2	679.0
Fluid 3	697.9	677.4	678.5	679.3	678.5	679.3
Fluid 4	680.4	678.7	679.8	680.9	679.8	680.6
Fluid 5	693.5	642.6	632.5	633.2	632.5	633.0
Fluid 6	699.6	683.4	686.5	687.5	686.5	687.3
Fluid 7	705.7	684.1	687.4	688.6	687.4	688.3
Fluid 8	718.4	685.7	689.7	691.0	689.7	690.7
Fluid 9	713.4	688.0	691.9	693.2	691.9	692.9
Fluid 10	706.6	685.7	688.4	689.5	688.4	689.2

Table D.2: Temperature [K] data for all correlations with friction at probes.

Probe	CFD	C1	C2	C3	C4	C5	Opt
Solid 1	735.2	744.8	740.6	736.2	740.7	741.0	735.9
Solid 2	686.5	682.6	683.5	685.2	683.5	683.8	684.8
Solid 3	655.6	638.0	635.6	644.1	635.6	636.0	643.8
Solid 4	546.8	537.0	549.2	549.3	549.2	549.3	549.2
Solid 5	580.8	568.6	573.0	573.1	573.0	573.1	573.1
Solid 6	656.5	650.2	660.4	663.9	660.4	659.6	659.3
Solid 7	740.4	753.7	732.0	726.6	732.0	728.2	732.1
Solid 8	786.1	814.0	770.6	759.0	770.7	762.5	770.8
Solid 9	893.5	895.9	896.0	896.0	896.0	896.0	896.0
Solid 10	845.2	847.4	847.4	847.4	847.4	847.4	847.4
Fluid 1	706.2	700.0	701.6	702.4	701.6	702.4	701.8
Fluid 2	704.8	694.1	693.9	694.2	693.9	694.7	693.6
Fluid 3	697.9	694.6	694.6	695.0	694.6	695.3	694.4
Fluid 4	680.4	696.3	696.1	696.9	696.1	696.9	696.2
Fluid 5	693.5	656.1	643.5	644.0	643.5	643.9	643.5
Fluid 6	699.6	701.4	703.4	704.1	703.4	704.2	703.5
Fluid 7	705.7	703.5	705.8	706.6	705.8	706.6	705.9
Fluid 8	718.4	706.9	709.7	710.6	709.7	710.6	709.8
Fluid 9	713.4	709.0	711.8	712.7	711.8	712.7	711.9
Fluid 10	706.6	703.1	704.6	705.4	704.6	705.4	704.8

E

Internal Heat Generation

Table E.1: Friction velocity (u_τ) and heat generation added to each thermal zone in the FEA model.

Thermal Zone	Friction Velocity [m/s]	Heat Generation [W]
Zone 1	3.3	7.1
Zone 2	1.9	0.7
Zone 3	1.2	0.1
Zone 4	3.1	1.7
Zone 5	3.1	1.5
Zone 6	4.4	5.2
Zone 7	8.1	44.2
Zone 8	10.0	115.5
Zone 9	10.9	174.0
Zone 10	5.5	12.7
Zone 11	3.8	9.2
Zone 12	2.8	3.3

F

HTC Values

Table F.1: HTC [$\mathrm{W\,m^{-2}\,K^{-1}}$] for all thermal zones for FEA correlations and CFD.

Thermal Zone	CFD	C1	C2	C3	C4	C5	Opt
Zone 1	788.8	385.8	558.4	783.8	557.8	557.8	783.8
Zone 2	473.1	354.7	477.6	671.2	477.7	477.7	671.2
Zone 3	434.0	438.6	391.8	551.7	392.6	392.6	551.7
Zone 4	809.3	487.5	780.4	780.4	780.4	780.4	780.4
Zone 5	735.3	465.6	774.6	774.6	774.6	774.6	774.6
Zone 6	764.5	432.4	865.7	1050.3	865.0	806.9	806.9
Zone 7	770.1	434.2	1125.2	1581.4	1125.5	1286.9	1125.5
Zone 8	833.9	449.5	1286.5	1804.4	1284.1	1674.3	1284.1
Zone 9	1058.6	433.5	1415.5	1983.0	1411.2	1790.9	1411.2
Zone 10	1216.6	397.1	397.1	397.1	397.1	397.1	397.1
Zone 11	774.6	458.8	458.8	458.8	458.8	458.8	458.8
Zone 12	701.1	366.7	366.7	366.7	366.7	366.7	366.7

Table F.2: Difference between correlation HTC [$\mathrm{W\,m^{-2}\,K^{-1}}$] and CFD for all thermal zones, in percent.

Thermal Zone	C1	C2	C3	C4	C5	Opt
Zone 1	-51.1	-29.2	-0.6	-29.3	-29.3	-0.6
Zone 2	-25.0	1.0	41.9	1.0	1.0	41.9
Zone 3	1.1	-9.7	27.1	-9.5	-9.5	27.1
Zone 4	-39.8	-3.6	-3.6	-3.6	-3.6	-3.6
Zone 5	-36.7	5.3	5.3	5.3	5.3	5.3
Zone 6	-43.4	13.2	37.4	13.1	5.5	5.5
Zone 7	-43.6	46.1	105.3	46.1	67.1	46.1
Zone 8	-46.1	54.3	116.4	54.0	100.8	54.0
Zone 9	-59.0	33.7	87.3	33.3	69.2	33.3
Zone 10	-67.4	-67.4	-67.4	-67.4	-67.4	-67.4
Zone 11	-40.8	-40.8	-40.8	-40.8	-40.8	-40.8
Zone 12	-47.7	-47.7	-47.7	-47.7	-47.7	-47.7

G

Fluid Bulk Temperature

Table G.1: Fluid point temperature used for CFD HTC calculations, and point coordinates.

Temperature [K]	**X [mm]**	**Y [mm]**	**Z [mm]**
705.4	104.0	187.0	-19.6
704.8	102.0	152.0	-16.0
697.9	102.0	110.0	-11.6
680.4	91.0	96.2	-10.1
693.5	49.0	96.2	-10.1
699.6	18.8	106.0	-11.2
704.1	8.7	144.0	-15.1
705.7	8.7	179.0	-18.8
718.4	2.6	214.0	-22.4
718.4	2.6	214.0	-22.4
713.4	36.0	210.0	-22.0
706.6	88.0	209.0	-21.9

DEPARTMENT OF MECHANICS AND MARITIME SCIENCES
CHALMERS UNIVERSITY OF TECHNOLOGY
Gothenburg, Sweden 2026
www.chalmers.se

CHALMERS
UNIVERSITY OF TECHNOLOGY